

# Fabrication, Testing and Characterization of MEMS Gyroscope

by

Ridha Almikhlafi

A thesis  
presented to the University of Waterloo  
in fulfillment of the  
thesis requirement for the degree of  
Master of Applied Science  
in  
Systems Design Engineering

Waterloo, Ontario, Canada, 2017

© Ridha Almikhlafi 2017

I hereby declare that I am the sole author of this thesis. This is a true copy of the thesis, including any required final revisions, as accepted by my examiners.

I understand that my thesis may be made electronically available to the public.

## Abstract

This thesis presents the design, fabrication and characterization of two Micro-Electro-Mechanical Systems (MEMS) vibratory gyroscopes fabricated using the Silicon-On-Insulator-Multi-User-MEMS-Process (SOIMUMPs) and Polysilicon Multi-User-MEMS-Process (PolyMUMPs). Firstly, relevant literature and background on static and dynamic analysis of MEMS gyroscopes are described. Secondly, the gyroscope analytical model is presented and numerically solved using Mathematica software. The lumped mass model was used to analytically design the gyroscope and predict their performance. Finite element analysis was carried out on the gyroscopes to verify the proposed designs.

Thirdly, gyroscope fabrication using MEMSCAP's SOIMUMPs and PolyMUMPs processes is described. For the former, post-processing was carried out at the Quantum Nanofab Center (QNC) on a die-level in order to create the vibratory structural elements (cantilever beam).

Following this, the PolyMUMPs gyroscopes are characterized optically by measuring their resonance frequencies and quality factor using a Laser Doppler Vibrometer (LDV). The drive resonance frequency was measured at 40 kHz and the quality factor as  $Q = 1$ . For the sense mode, the resonance frequency was measured at 55 kHz and the unity quality factor as  $Q = 1$ . The characterization results show large drive direction motions of 100  $\mu\text{m/s}$  in response to a voltage pulse of 10V. The drive pull-in voltage was measured at 19V. Finally, the ratio of the measured drive to sense mode velocities in response to a voltage pulse of 10 V was calculated at 1.375.

## Acknowledgements

First of all, I would like to thank my God for providing me the guidance, strength, and patience to complete this thesis work and, hence, the MASc degree successfully. I would like to express my deep sincere appreciation to my supervisor, Prof. Eihab Abdel-Rahman for his time, guidance, support, and encouragement throughout this work. Also, I express my thanks to my co-supervisor Prof. Mustafa Yavuz for his assistance in the fabrication work. I would like to thank my committee reader Prof. Nasser Azad for his time in evaluating my work. I am also very grateful to my colleagues Dr. Sangtak Park, Dr. Mahmoud Khater, Ayman Alneamy, Majed Alghamdi, Abdulaziz Radwan, Hamid Nafissi and Ahmad Kamal for their suggestions, cooperations and support throughout my MASc degree.

I should also thank King Abdulaziz City for Science and Technology (KACST) for their scholarship and funding me during my Master degree.

Finally, I have to express my very profound gratitude to my parents for their sacrifices to help me reach this level of education. My thanks also go to my brothers and sisters for their encouragement and support. Without them, I could not be able to achieve it.

# Table of Contents

List of Tables	vii
List of Figures	viii
Nomenclature	xi
<b>1 Introduction</b>	<b>1</b>
1.1 Motivation . . . . .	1
1.2 Static Analysis of MEMS . . . . .	2
1.2.1 Hookes Law . . . . .	2
1.2.2 Series and Parallel Springs . . . . .	2
1.2.3 Spring Stiffness . . . . .	3
1.3 Dynamic Analysis of Gyroscopes . . . . .	4
1.3.1 Mechanical Oscillators . . . . .	5
1.3.2 Capacitive Actuation and Detection . . . . .	7
1.4 MEMS Vibratory Gyroscopes . . . . .	10
1.5 Research Objectives and Thesis Organization . . . . .	13
1.6 Thesis Contribution . . . . .	14
<b>2 Cantilever Beam Gyroscopes</b>	<b>15</b>
2.1 Gyroscope Design . . . . .	15

2.2	Lumped Mass Model . . . . .	15
2.3	Model Results . . . . .	18
2.4	Modal Analysis . . . . .	21
<b>3</b>	<b>Gyroscope Fabrication</b>	<b>23</b>
3.1	SOIMUMPs Gyroscopes . . . . .	23
3.1.1	Manufacturing Layout . . . . .	23
3.1.2	Process Flow . . . . .	25
3.2	Post-processing of SOIMUMPs . . . . .	26
3.2.1	Height Measurement . . . . .	27
3.2.2	Silicon Etching . . . . .	28
3.2.3	Die Cleaning . . . . .	28
3.2.4	Wet Etching of Silicon Dioxide . . . . .	29
3.2.5	Silicon Dioxide Deposition . . . . .	30
3.2.6	Photolithography . . . . .	31
3.2.7	Dry Etching of Silicon Dioxide . . . . .	31
3.2.8	Structural Layer Deposition . . . . .	32
3.3	PolyMUMPs Gyroscope . . . . .	34
<b>4</b>	<b>Test and Characterization</b>	<b>36</b>
4.1	Optical Detection . . . . .	36
4.2	Characterization of Drive Mode . . . . .	37
4.2.1	Pull-in Voltage . . . . .	38
4.3	Characterization of Sense Mode . . . . .	39
<b>5</b>	<b>Conclusions and Future Work</b>	<b>43</b>
5.1	Conclusions . . . . .	43
5.2	Future Work . . . . .	44
	<b>Bibliography</b>	<b>45</b>

# List of Tables

1.1	Comparison of Actuation Mechanisms in MEMS . . . . .	11
2.1	Dimensions and material properties of the fabricated cantilever beam gyroscopes . . . . .	16
2.2	Simulated natural frequencies for the drive and sense modes. . . . .	22
3.1	Elements of the SOIMUMPs gyroscope . . . . .	24

# List of Figures

1.1	Springs connected (a) in parallel and (b) in series . . . . .	2
1.2	Rod extension due to $P_z$ . . . . .	4
1.3	The lumped mass-spring-damper model . . . . .	5
1.4	DOF resonator . . . . .	6
1.5	Comb-drive actuator . . . . .	7
1.6	Variable-gap detector . . . . .	8
1.7	Variable-area detector . . . . .	9
1.8	Variable-gap comb-finger capacitor . . . . .	9
1.9	Tuning fork gyroscope . . . . .	12
1.10	Micromachined vibrating ring-type gyroscope . . . . .	13
2.1	Cantilever beam MEMS gyroscope . . . . .	16
2.2	Schematic diagram of the drive and sense modes . . . . .	17
2.3	The displacement-voltage relationship for the PolyMUMPs gyroscope . . . . .	18
2.4	The frequency-response curves of the drive and sense modes for the PolyMUMPs gyroscope . . . . .	19
2.5	The displacement-voltage relationship for the SOIMUMPs gyroscope . . . . .	20
2.6	The frequency-response curves of the drive and sense modes for the SOIMUMPs gyroscope . . . . .	20
2.7	Block diagram of ANSYS Modal Analysis solution . . . . .	21
2.8	The first out-of-plane and in-plane bending modes of the PolyMUMPs gyroscope . . . . .	21



2.9	The first out-of-plane and in-plane bending modes of the SOIMUMPs gyroscope . . . . .	22
3.1	A snapshot of the overall L-Edit layout . . . . .	24
3.2	SOIMUMPs Process Flow . . . . .	25
3.3	SEM picture of the ‘as-received’ SOIMUMPs die . . . . .	26
3.4	Height measurements by used Dektak 150 Surface Profiler . . . . .	27
3.5	Cross sectional view showing all layers . . . . .	27
3.6	DRIE Etching of the Silicon . . . . .	28
3.7	(a) A schematic of the cross-sectional view before and after plasma ashing and (b) SEM picture of the die after plasma ashing . . . . .	29
3.8	(a) A schematic cross-sectional view and (b) SEM picture of the die after removing residual Si walls using Piranha cleaning . . . . .	29
3.9	(a) Schematic of the die before and after buffered oxide etch of SiO <sub>2</sub> and (b) SEM picture of the result . . . . .	30
3.10	(a) Schematic and (b) SEM picture of the die after PECVD of SiO <sub>2</sub> . . . . .	30
3.11	Lithography process . . . . .	31
3.12	SiO <sub>2</sub> etching using RIE . . . . .	32
3.13	Deposition and patterning of the gyroscope structure . . . . .	32
3.14	Process flow for post processing of SOIMUMPs dies . . . . .	33
3.15	PolyMUMPs gyroscope fabrication steps . . . . .	34
3.16	SEM pictures of the PolyMUMPs gyroscope . . . . .	35
4.1	Experimental Setup . . . . .	36
4.2	(a) SEM of the PolyMUMPs gyroscope. (b) Schematic diagram of drive mode actuation . . . . .	37
4.3	A screen capture of the laser vibrometer interface showing the frequency-response (top panel) and the time-domain response (bottom panel) of the drive mode velocity under a pulse train excitation . . . . .	38
4.4	Pull in voltage . . . . .	39

4.5	The chip carrier placed on the tilt stage . . . . .	40
4.6	(a) SEM of the PolyMUMPs gyroscope. (b) Schematic diagram of sense mode actuation . . . . .	41
4.7	A screen capture of the laser vibrometer interface showing the frequency-response (top panel) and the time-domain response (bottom panel) of the sense mode velocity under a pulse train excitation . . . . .	41
4.8	Plots of the (a) drive and (a) sense modes frequency response under a pulse train . . . . .	42

# Nomenclature

The following notations are used throughout the text and other notations are used at their relevant positions:

$V$	Applied voltage
$F_c$	Coriolis force
$m$	Mass per unit length cantilever beam gyroscope
$F_{es}$	Electrostatic force Spring stiffness
$C$	Capacitance
$F$	Force
$L_b$	Cantilever Beam length
$h_b$	Cantilever Beam thickness
$b_b$	Cantilever Beam width
$DOF$	Degree of freedom
$Q_e$	Electrical charging
$Q$	Quality factor
$F_{es}$	Electrostatic force
$S$	strain
$d$	Gap

$L_p$	Plate length
$h_p$	Plate thickness
$b_p$	Plate width
$U_c$	Potential energy
$V_{pin}$	Pull in voltage
$t$	Time scaling
$T$	Stress
$BW$	Bandwidth
$E$	Youngs modules

# Chapter 1

## Introduction

### 1.1 Motivation

Micro-Electromechanical Systems (MEMS), as the name implies, are miniaturized (relatively very small) devices integrating electrical and mechanical components. The fabrication of MEMS emerged thanks to the maturity of the CMOS fabrication technology. Such standardization in terms of materials, process and equipment used has enabled the development of low-power and low-cost sensors and actuators. Our area of interest in this work is the motion sensor, in particular the inertial sensors, which are used to measure the rotation rate. Typical devices employing MEMS inertial sensors are gyroscopes and accelerometers. They specifically measure the angle with respect to the body's inertial reference frame.

Recently, the MEMS inertial sensor market has grown dramatically due to the rise of mobile communication platforms, the introduction of Internet of Things (IOT), augmented reality and newly developed game-console joysticks [1, 3]. Hence, the demand for MEMS gyroscopes in the sensor market has risen significantly and is expected to grow even further in the upcoming years [4].

Gyroscopes can be actuated electrostatically, piezo-electrically or by laser. Our work here focuses on the electrostatic MEMS vibratory gyroscope, which is a simpler form of the conventional gyroscope. Its principle of operation is described in section 1.3.

## 1.2 Static Analysis of MEMS

### 1.2.1 Hookes Law

Hookes law of elasticity states that spring extension  $x$  is directly proportional to the load applied  $f$  to it. It is represented mathematically by:

$$F = -kx \quad (1.1)$$

where  $k$  is the spring stiffness. The minus sign indicates that the spring has a restoring force opposite in direction to the applied force. For many materials, this law is applicable only within a limited linear range. Typically, the critical point at which the relationship between the force and displacement becomes nonlinear and the elastic limit are indistinguishable [4]. In our gyroscope design, we limit our interest to the linear region since the displacements are relatively small.

### 1.2.2 Series and Parallel Springs

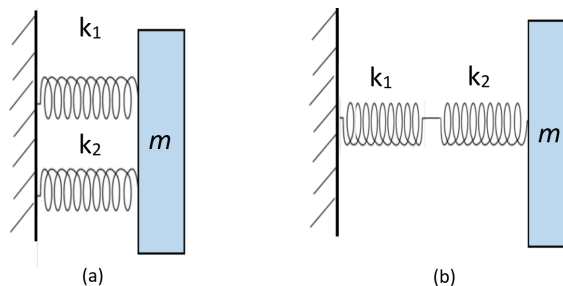


Figure 1.1: Springs connected (a) in parallel and (b) in series

As the design of gyroscopes involves nontrivial architectures, it is essential to understand the way springs behave when they are combined. In case of series connection between two springs with stiffness  $k_1$  and  $k_2$ , Figure 1.1 (b), the applied force acts on both springs. The total displacement can be written as:

$$x_t = x_1 + x_2 = \frac{F}{k_1} + \frac{F}{k_2} \quad (1.2)$$

Equivalently, we can write

$$F = k_{eq}x_t \quad \text{where} \quad k_{eq} = \frac{k_1 k_2}{k_1 + k_2} \quad (1.3)$$

On the other hand, when two springs with stiffness  $k_1$  and  $k_2$  are connected in parallel, as illustrated in Figure 1.1 (a), the displacement is common to both springs and the total force can be written as

$$F_t = F_1 + F_2 = k_1 x + k_2 x \quad (1.4)$$

Equivalently, we can write

$$F_t = k_{eq} x \quad (1.5)$$

where  $k_{eq} = k_1 + k_2$ .

### 1.2.3 Spring Stiffness

Spring stiffness varies depending on its material and geometry. Therefore, the stress-strain relationship underlying material stiffness is introduced here. Stress  $T$  is defined as the total force  $P$  applied per unit area  $A$

$$T = \frac{P}{A} \quad (1.6)$$

The geometry of a spring governs the magnitude of stress. Therefore, the direction of force as well as the plane of the area must be identified. In Cartesian coordinates, stress can be written in the form.

$$T_x = \frac{F_x}{A_x}, \quad T_y = \frac{F_y}{A_y}, \quad T_z = \frac{F_z}{A_z} \quad (1.7)$$

Positive  $T$  in Figure 1.4 indicates that the spring is exposed to tensile stress whereas negative  $T$  means stress is compressive.

Strain is the ratio of the relative change in spring length to its total length.

$$S = \frac{\Delta l}{l} \quad (1.8)$$

Similar to stress, strain can be written in Cartesian components as:

$$S_x = \frac{\Delta l_x}{l_x}, \quad S_y = \frac{\Delta l_y}{l_y}, \quad S_z = \frac{\Delta l_z}{l_z} \quad (1.9)$$

Material stiffness, Young's modulus, is the ratio of the uniaxial stress over the uniaxial strain as long as Hooke's law applies.

$$E = \frac{T}{S} \quad (1.10)$$

Further,

$$E_x = \frac{T_x}{S_x} \quad , \quad E_y = \frac{T_y}{S_y} \quad , \quad E_z = \frac{T_z}{S_z} \quad (1.11)$$

The units of stress  $T$  and Young's modulus are  $\text{N/m}^2$  or Pascal (Pa) while strain is unitless. Young's modulus for most solids is in the range of mega to giga Pascal (MPa to GPa).

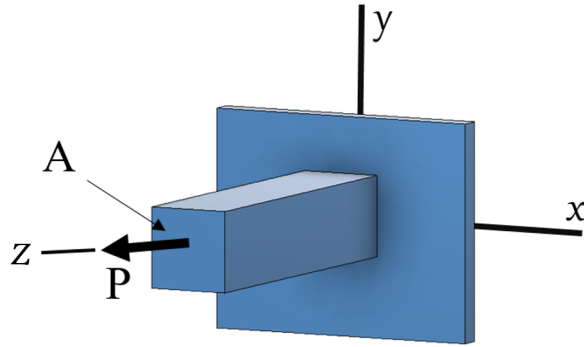


Figure 1.2: Rod extension due to  $P_z$

The rod in Figure 1.2 is extended in the z-direction 'longitudinally'. Because of material continuity, this causes compression in the x- and y-direction 'transversally'. This effect is referred to as Poisson's effect. Quantitatively, it is the ratio between forced longitudinal strain and unforced transverse strains

$$\nu = -\frac{S_x}{S_z} = -\frac{S_y}{S_z} \quad (1.12)$$

The negative sign means that shrinkage occurs in the transverse directions due to extension in the longitudinal direction. For most materials,  $\nu$  ranges between 0.1 and 0.4 [4].

### 1.3 Dynamic Analysis of Gyroscopes

Next, we define linear mechanical oscillators and their resonance as they relate to gyroscopes. We also describe the drive and sense modes of vibratory gyroscopes.



### 1.3.1 Mechanical Oscillators

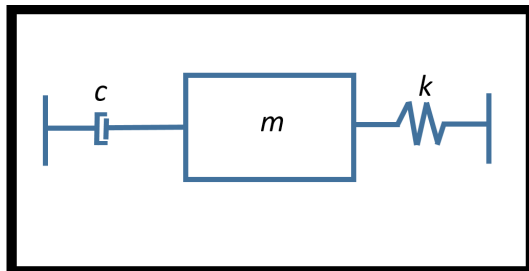


Figure 1.3: The lumped mass-spring-damper model

The equation of motion of a mechanical oscillator can be written as:

$$m\ddot{x} + c\dot{x} + kx = F(t) \quad (1.13)$$

where  $m$  is the mass and  $k$  is the spring stiffness. The damping coefficient  $c$  can also be expressed as:  $c = 2\xi m\omega_n$ , where  $\xi$  is the damping ratio and  $\omega_n = \sqrt{k/m}$  is the angular natural frequency. Dividing equation (1.13) by  $m$  yields:

$$\ddot{x} + 2\xi\omega_n\dot{x} + \omega_n^2x = \frac{F(t)}{m} \quad (1.14)$$

Converting the above equation into Laplace domain, we get:

$$\frac{X(s)}{F(s)} = \frac{1}{s^2 + 2\xi\omega_n s + \omega_n^2} \quad (1.15)$$

The gyroscope vibrates when driven by a harmonic force  $F(t) = F_o \sin \omega t$ . In response to this, its displacement in time-domain takes the form  $x(t) = x_o \sin(\omega - \phi)$  where:

$$x_o = \frac{F_o}{k\sqrt{[1 - (\frac{\omega}{\omega_n})^2]^2 + [2\xi\frac{\omega}{\omega_n}]^2}}, \quad \phi = \tan^{-1} \frac{2\xi\omega\omega_n}{\omega_n^2 - \omega^2} \quad (1.16)$$

Resonance occurs when the driving and the damped natural frequencies are equal  $\omega = \omega_d$  where

$$\omega_d = \omega_n \sqrt{1 - \zeta^2} \quad (1.17)$$

At resonance, the response amplitude attains a maximum of:

$$x_o = \frac{F_o}{2k\xi} = \frac{F_o}{c\omega_n} \quad (1.18)$$

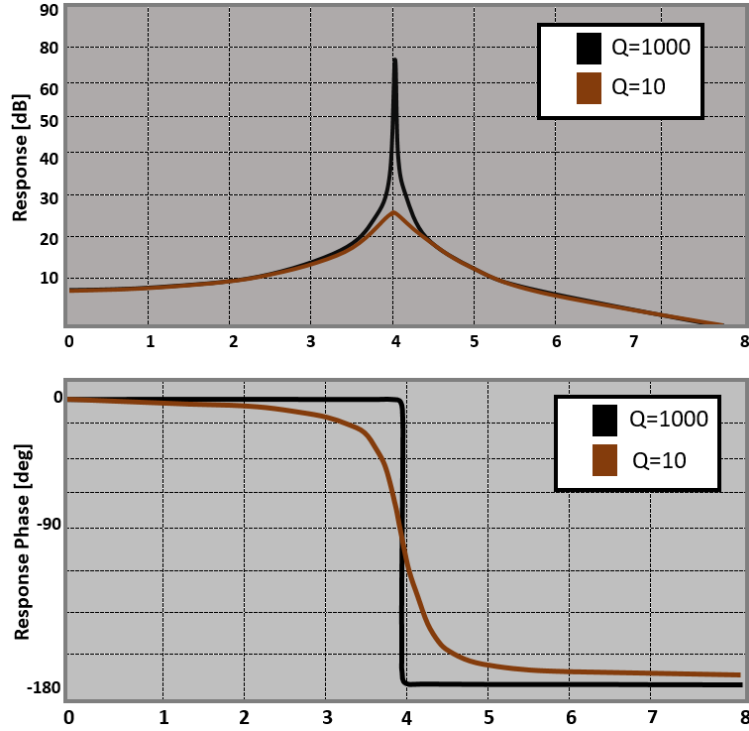


Figure 1.4: DOF resonator .

as can be seen in Figure 1.4.

The resonance frequency can be identified by observing the phase spectrum of a gyroscope. Assuming the phase angle is initially  $\phi = 0^\circ$ , it will ultimately approach  $-180^\circ$  in a frequency sweep past the natural frequency. The phase shift reaches exactly  $\phi = -90^\circ$  at the resonance  $\omega = \omega_n$ .

In MEMS literature, damping is frequently expressed in terms of the Quality Factor  $Q$ . It is related to the damping ratio by:

$$Q = \frac{1}{2\xi} \quad (1.19)$$

As  $Q$  increases, the transition region from  $0^\circ$  to  $-180^\circ$  becomes sharper and the peak response become more pronounced as illustrated in Figure 1.4 [1]. The half-power bandwidth of the gyroscope, range of frequencies over which the response carries at least half of the peak power, is related to the quality factor  $Q$  by:

$$BW = \frac{\omega_n}{Q} \quad (1.20)$$

## 1.3.2 Capacitive Actuation and Detection

### Longitudinal Comb-Drive Actuator

In longitudinal comb-drive actuators, two parallel sets of electrodes move longitudinally with respect to each other as the capacitive gap between them  $d$  remain fixed. Figure 1.5 shows a schematic view of a comb-drive actuator. The finger-to-finger capacitance is given by [4]:

$$C = \epsilon N \frac{h(l+x)}{d} + C_f \quad (1.21)$$

where  $\epsilon$  is the permittivity constant,  $N$  is the number for finger-to-finger units,  $l$  is the initial overlap length between fingers,  $h$  is the finger height,  $x$  is the finger displacement,  $C_f$  is the fringe capacitance between the two fingers.

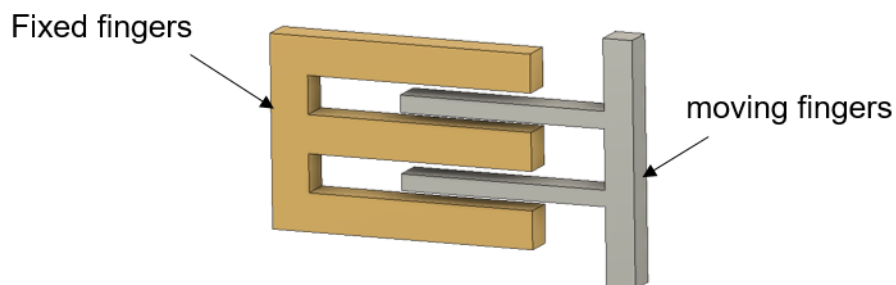


Figure 1.5: Comb-drive actuator

The electrostatic force acting on the actuator can be derived from Castegliano's First Theorem as the change of electrostatic potential energy with respect to displacement

$$F_e = \frac{d}{dx} \left( \frac{1}{2} C V^2 \right) \quad (1.22)$$

where  $V$  is the voltage across the comb-finger capacitor electrodes. For a voltage controlled actuator, where  $V$  remains constant over time, using Eq 1.21 in 1.22 yields:

$$F_e = \epsilon N \frac{h}{2d} V^2 \quad (1.23)$$

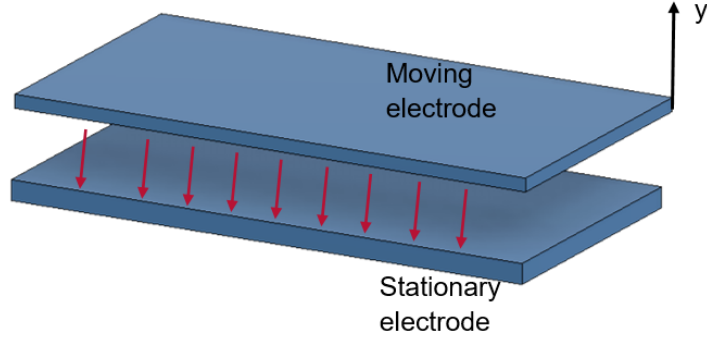


Figure 1.6: Variable-gap detector

### Variable-Gap Detector

Variable-gap capacitors are very popular among MEMS designers as motion detectors due to their high sensitivity, typically on the order of a few  $(\frac{\Delta pf}{\Delta \mu m})$  [4]. Figure 1.6 illustrates a variable-gap capacitor where parallel electrode plates are oriented perpendicular to the direction of motion. Assuming rigid electrode plates and ignoring fringing field, the change in capacitance is

$$\Delta C = \epsilon_o \frac{tL}{d-y} - \epsilon_o \frac{tL}{d} = \epsilon_o tL \frac{y}{d^2 - dy} \quad (1.24)$$

where  $L$  and  $w$  are the plate length and width, usually in tens of  $\mu m$ , and  $y$  is the measured displacement. Assuming small displacements ( $y \ll d$ ), the capacitance change can be approximated by

$$\Delta C \approx \epsilon_o \frac{tL}{d^2} y \quad (1.25)$$

## Variable-Area Detector

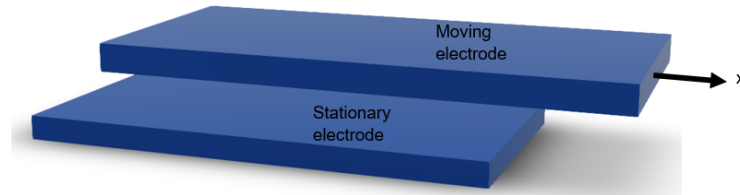


Figure 1.7: Variable-area detector

Variable area capacitors, Figure 1.7, are also used to detect motion in MEMS. They have superior linearity compared to variable-gap detectors. For this reason, they are used when the magnitude of motion is relatively large. In this case, the change in capacitance is given by:

$$\Delta C = \epsilon_o \frac{t(l+x)}{d} - \epsilon_o \frac{tl}{d} = \epsilon_o \frac{t}{d} x \quad (1.26)$$

## Differential Sensing

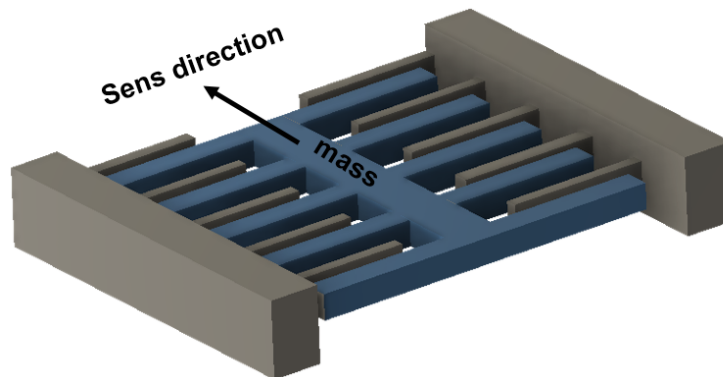


Figure 1.8: Variable-gap comb-finger capacitor

Differential sensing is used to minimize the effects parasitic and fringe capacitances, thereby enhancing sensitivity. It also minimizes the nonlinear effects of the finger tip capacitance, thus improving linearity. Figure 1.8 depicts such a configuration; a gap increase

between the moving fingers and the right-hand side of the stationary fingers is associated with a gap decrease with respect to the left-hand side of the stationary finger. Considering  $N$  fingers, the left and right-hand sides capacitances are calculated as [1]

$$C_{s+} = N \frac{\epsilon_o t L}{d - y} \quad C_{s-} = N \frac{\epsilon_o t L}{d + y} \quad (1.27)$$

Using Eq. (2.2), the differential capacitance is approximately written as:

$$\Delta C = C_{s+} - C_{s-} \approx 2N \frac{\epsilon_o t L}{d^2} y \quad (1.28)$$

## 1.4 MEMS Vibratory Gyroscopes

MEMS Vibratory Gyroscopes (MVGs) as the name implies are micromachined devices using their own vibrations to measure the rate of rotation. They exploit the Coriolis effect caused by the interaction of a translational velocity  $\dot{\vec{x}}$  and an angular velocity  $\vec{\Omega}$  and represented by the Coriolis force:

$$F_c = 2m\vec{\Omega} \times \dot{\vec{x}} \quad (1.29)$$

where  $m$  is the moving mass.

A ‘drive mode’ generates oscillatory translational momentum ( $m\dot{x}$ ) along the x-axis. When angular velocity  $\Omega_z$  occurs around the z-axis, a Coriolis force

$$F_c = 2m\Omega_z \dot{x} \quad (1.30)$$

is generated which results in oscillatory motions along the y-axis. The resulting motion, called the sense mode, is dependent on the size of the drive mode in oscillations, amplitude of  $\dot{x}(t)$ , therefore it is desirable to operate the drive and sense modes at resonance in order to exploit dynamic amplification to maximize drive  $x(t)$  and sense  $y(t)$  motions [1]. The drive and sense motions are described by Eqs (1.13) through (1.19). Table 3.1 below summarizes these relations where  $F_d$  is the amplitude of the drive force.

The MVG works as follows: The drive axis is excited with a small ac signal at a pre-determined frequency to vibrate continuously along the x-axis. When an external rotation  $\Omega$  acts around the z-axis, a second (sense) oscillation is induced due to the Coriolis effect along the y-axis. The proof mass motions in the sense direction  $y(t)$  can be used to estimate the angular rotation  $\Omega$  of the gyroscope base.

Table 1.1: Comparison of Actuation Mechanisms in MEMS

	Drive Mode	Sense Mode
Equation of Motion	$m_d \ddot{x} + c_d \dot{x} + k_d x = F_d \sin(\omega t)$	$m_s \ddot{y} + c_s \dot{y} + k_s y = F_c$
Amplitude	$x_o = \frac{F_d}{k_d} Q_d ; \quad \omega = \omega_d$	$y_o = 2\Omega_z \frac{Q_d}{\omega_d} \frac{F_d}{\sqrt{[1 - (\frac{\omega_d}{\omega_s})^2]^2 + [\frac{1}{Q_s} \frac{\omega_d}{\omega_s}]^2}}$
Phase	$\phi_d = \tan^{-1} \frac{\omega_d \omega}{Q_d(\omega_d^2 - \omega^2)}$	$\phi_s = \tan^{-1} \frac{\omega_s \omega_s}{Q_d(\omega_s^2 - \omega_d^2)} + \phi_d$

Put differently, vibratory gyroscopes are composed of two MEMS devices: a large-amplitude high-Q resonator and a high sensitivity sub- $\mu\text{g}$  accelerometer. They have to work together in order to sense angular velocity.

Several electromechanical transduction mechanisms are widely, including electrostatic [19], piezoelectric [16], and electromagnetic [17] actuation methods. The latter two are commonly used at a macro-scale as they provide relatively energy density. As of yet, they have not been successfully downscaled to micro-dimensions and silicon-based fabrication technology since they lack standard materials. For this reason, electrostatically actuated gyroscopes, which require no special materials, have become popular. Typically, electrostatic MEMS gyroscopes used comb-finger actuation.

Surface micromachining is based on the deposition and etching of thin layers,  $\sim 2\mu\text{m}$ , on the top of the substrate. An advantage of surface micromachining is its compatibility with conventional IC fabrication technology, hence allowing single-chip fabrication. However, surface micromachined gyroscopes suffer from relatively low inertial mass, preventing them from attaining the low enough noise floor necessary for high-end navigation applications. As a consequence, the majority of MVGs are developed using high-aspect-ratio bulk microfabrication processes, such Silicon on Glass (SOG), Silicon on Insulator (SOI) and LIGA technologies [46].

MVGs are built using various microfabrication technologies, including surface micromachining [19], bulk micromachining and wafer bonding [22], electroplating and LIGA [24, 25], combined surface-bulk micromachining [27] as well as the recently developed EFAB technology. The designs of MVGs can be classified into three basic configurations, namely tuning forks, vibrating rings, and vibrating plates [19], [30]-[46]

The classical example of MVGs is the tuning fork design, for example [50] developed a tuning fork gyroscope similar to that shown in Figure 1.9. It contains a pair of proof masses

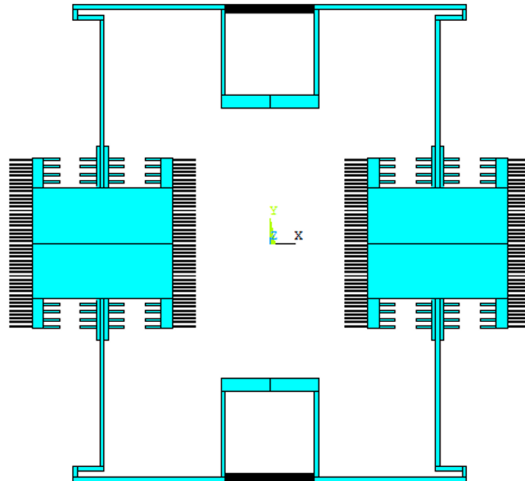


Figure 1.9: Tuning fork gyroscope

coupled to each other via mechanical suspension. The masses vibrate in their out-of-phase mode. When a rotation around the axis perpendicular to the device plan is present, the Coriolis force cause the masses to vibrate in opposite direction to each other along an axis perpendicular to the drive axis [12, 13]. The main advantage of tuning fork gyroscopes is that they reject common-mode input, such as linear acceleration. However, challenges arise due to cross-coupling between the inertial masses and fabrication imperfections leading to asymmetry in the mechanical suspension system.

Cross-coupling and asymmetry lead to so-called the ‘mechanical quadrature error’. The quadrature signal is in phase with the drive signal; but  $90^\circ$  out-of-phase with the Coriolis force. This quadrature signal can easily dominate the output of a gyroscope due to the small magnitude of the Coriolis force. Nevertheless, the problem of quadrature signal can be alleviated by very careful micromachining and by applying electrostatic forces to null deflections resulting from quadrature error [30]. Another source of cross-coupling are fabrication imperfections of the interdigitated comb fingers, which generate zero rate output in the sense mode of the gyroscope.

To overcome these problems, several approaches have been investigated to provide for frequency matching between the drive and sense modes and to improve robustness against cross-coupling errors. Najafi et al. [24] proposed a micromachined gyroscope based on a vibrating ring structure as that shown in Figure 1.10.

Several methods have been investigated to reduce mechanical noise and to enhance the readout signal. In order to increase the mass beyond surface micromachined gyroscopes



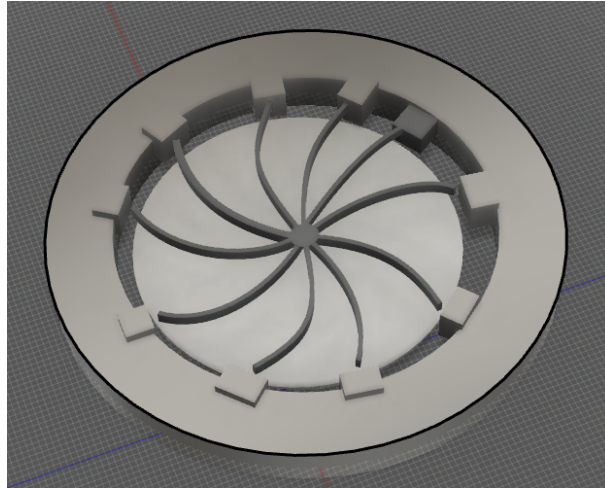


Figure 1.10: Micromachined vibrating ring-type gyroscope

and increase capacitances in capacitively sensed gyroscopes, high-aspect-ratio (HAR) bulk micromachining techniques have been used. Several companies like STS, Alcatel and Plasmatherm have developed the technology for deep and narrow trench etching in single-crystalline silicon. Deep etching with aspect ratio of 50:1 for hundreds of micron thick silicon can be achieved [42],[43]. This technology greatly simplifies the design of high-performance gyroscopes by making the fabrication of high aspect ratio suspension beams and inertial masses possible.

## 1.5 Research Objectives and Thesis Organization

This thesis contains five chapters arranged as follows:

**Chapter 1** reviews the literature on a MEMS Vibratory Gyroscopes.

**Chapter 2** presents the systems parameters for cantilever beam gyroscopes, their electrostatic drive and sense mechanisms, as well as FEM and analytical models of the gyroscopes.

**Chapter 3** presents the fabrication process of the gyroscopes. Two fabrication platform were used: SOIMUMPs and POLYMUMPs.

**Chapter 4** presented the experimental characterization of the gyroscope prototypes including their natural frequencies and quality factors.

**Chapter 5** includes a discussion and conclusions of this research as well as recommendations for future work.

## 1.6 Thesis Contribution

The main contribution of this research is exploring the feasibility of using various micro fabrication techniques to realize cantilever beam gyroscope and comparison of the fabricated gyroscopes performance to that of gyroscopes reported previously by Effa et al. [61]. Specifically, the contributions of this thesis fall under three categories:

1. Fabrication of gyroscopes utilizing post-processing of SOIMUMPs technology.
2. Design of gyroscope fabricated using the standard PolyMUMPs technology.
3. Characterization of fabricated gyroscopes.

# Chapter 2

## Cantilever Beam Gyroscopes

In this chapter, the theory of the cantilever beam gyroscopes is presented. Section 2.1 presents a linear model for the drive and sense modes coupled by the Coriolis force.

### 2.1 Gyroscope Design

The design of a cantilever beam gyroscope, Figure 2.1, is another approach towards measuring the angular displacement or rate by using the free vibration of a suspended mass. The gyroscope is composed of two sets of electrodes, an anchor, a beam and a suspended mass. The dimensions of the beam and mass are critical in fine tuning the desired resonant frequency. Also, this design uses frequency-domain (FM) sensing, which measures the angular rate by detecting the difference between the natural frequencies of two closely spaced global vibration modes. In comparison with the standard time-domain (AM) sensing, FM sensing has higher sensitivity, better linearity and lower noise floor[61].

### 2.2 Lumped Mass Model

Electrostatic actuation requires low power. Because of its high impedance, at relatively low frequencies the actuated devices draw very low current. Further, its fabrication process is fairly standardized and its materials are widely available. In principle, electrostatic actuators are made of two plates with opposite charges that attract each other [63].

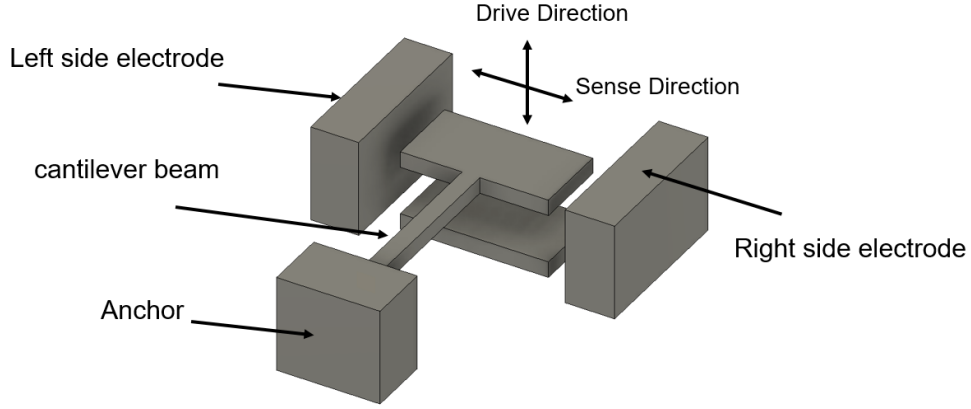


Figure 2.1: Cantilever beam MEMS gyroscope

Table 2.1: Dimensions and material properties of the fabricated cantilever beam gyroscopes

Parameters	SOI	PolyMUMPs
Beam length, $\mu\text{m}$	282	190
Beam width, $\mu\text{m}$	9.5	20
Bottom capacitive gap $d_b$ ( $\mu\text{m}$ )	2	2
Side capacitive gap $d_s$ , $\mu\text{m}$	3	6.5
Microplate length, $\mu\text{m}$	96	40
Microplate width, $\mu\text{m}$	140	40
Layer thickness, $\mu\text{m}$	10	2
Density $\rho$ ( $\text{kg}/\text{m}^3$ )	2340	2340
Youngs modules $E$ (GPa)	300	160

The drive mode of a gyroscope is actuated by the bottom electrode and shown schematically in Figure 2.2. When the gyroscope is driven at resonance, its motions reach a maximum which maximizes the Coriolis force, as per Eq. (1.30), and therefore energy transfer from the drive to the sense mode [13].

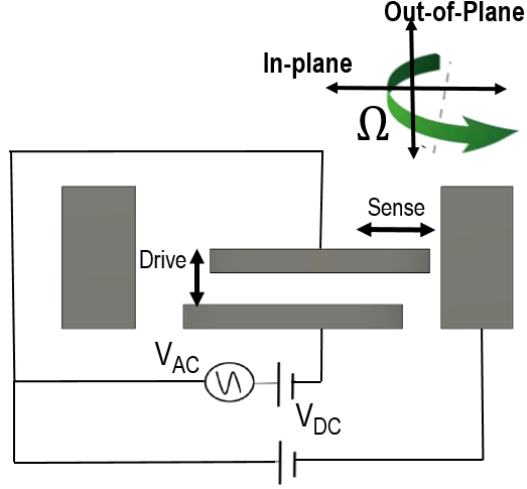


Figure 2.2: Schematic diagram of the drive and sense modes

The gyroscopes operation can be modeled as a two-degree-of-freedom (2 DOF) mass-spring-damper system [13, 16]. The first DOF is the displacement of the micro-plate center in the drive direction  $x(t)$  whereas the second DOF is the displacement of the micro-plate center in sense direction  $y(t)$ . The latter is orthogonal to the former. When the drive mode is operated in forced vibrations, its equation of motion is given by :

$$m\ddot{x} + c_d\dot{x} + k_d x = \frac{1}{2} \frac{\epsilon A_b V_d^2}{(d_b - x)^2} \quad (2.1)$$

where  $m$  is the equivalent mass,  $c_d$  is the drive mode viscous damping coefficient,  $k_d$  is the equivalent stiffness in the drive direction,  $A_b$  is the common area between the micro-plate and the bottom electrode and  $V_d(t)$  is the actuation voltage of the drive mode. The gyroscope output is a function of the drive motions  $x(t)$ , which requires closed loop control to maintain the desired amplitude constant. In our case, we will forgo closed loop control since our goal is to investigate the feasibility of cantilever beam gyroscopes.

Sense mode motions occur in the presence of an angular rate  $\Omega$  and drive oscillations  $x(t)$ , Figure 2.2. When the sense mode is operated in forced vibrations, its equation of motion is given by:

$$m\ddot{y} + c_s\dot{y} + k_s y = 2m\Omega\dot{x} + \frac{1}{2} \frac{\epsilon A_s V_s^2}{(d_s - x)^2} \quad (2.2)$$

Similarly,  $c_s$  is the viscous damping coefficient,  $k_s$  is the equivalent stiffness in the sense direction,  $A_s$  is the common area between the micro-plate and the side electrodes and  $V_s$

is the voltage in the sense mode. The detection system requires a capacitance to voltage conversion followed by digitization. In the case of AM modulated gyroscopes, an additional signal processing step is required where the output motion is amplitude demodulated in order to extract the angular rate.

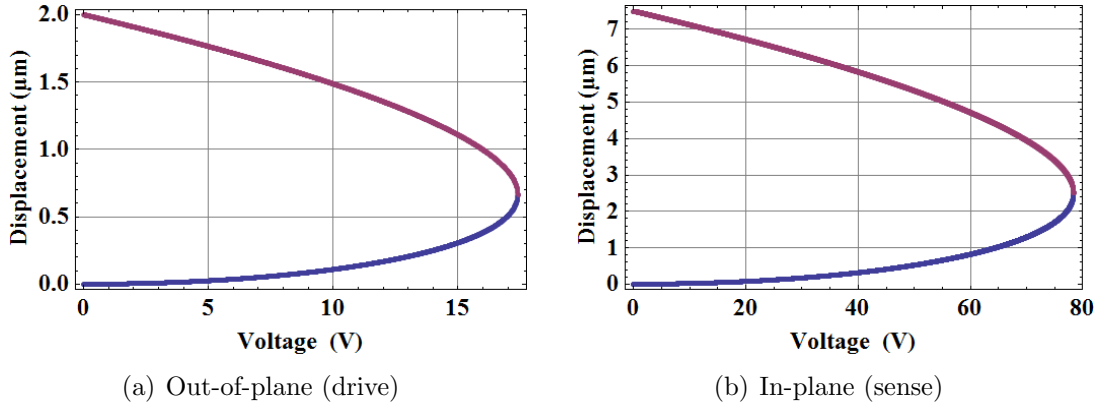


Figure 2.3: The displacement-voltage relationship for the PolyMUMPs gyroscope

## 2.3 Model Results

Setting the time derivatives in the equations of motion, Eqs. (2.1) and (2.2), equal to zero and solving the resulting algebraic equation for the corresponding static deflection  $x$ , we obtain the static response of the gyroscope. Figures 2.3 (a) and (b) show the relationship between the out-of-plane and in-plane, the drive and sense, deflections of the microplate center and the dc voltage of the bottom electrode and one of the side electrodes, respectively, for the PolyMUMPs gyroscope. Deflection increases with voltage until a saddle-node bifurcation point, the pull-in point. A stable and an unstable equilibrium exist corresponding to each dc voltage value. The stable (blue line) and unstable (red line) branches of solutions annihilate each other at the bifurcation point. No equilibrium points exist for dc voltage values larger than the pull-in voltage, and hence the gyroscope loses stability. The pull-in voltage was calculated as 19 V for the out-of-plane direction (drive mode) where the electrostatic force overcomes the mechanical spring force. The in-plane pull-in voltage (sense mode) was calculated as 79 V. The difference in pull-in voltage is due to the larger capacitive gap  $d_s$  and smaller area  $A_s$  of the sense electrodes.

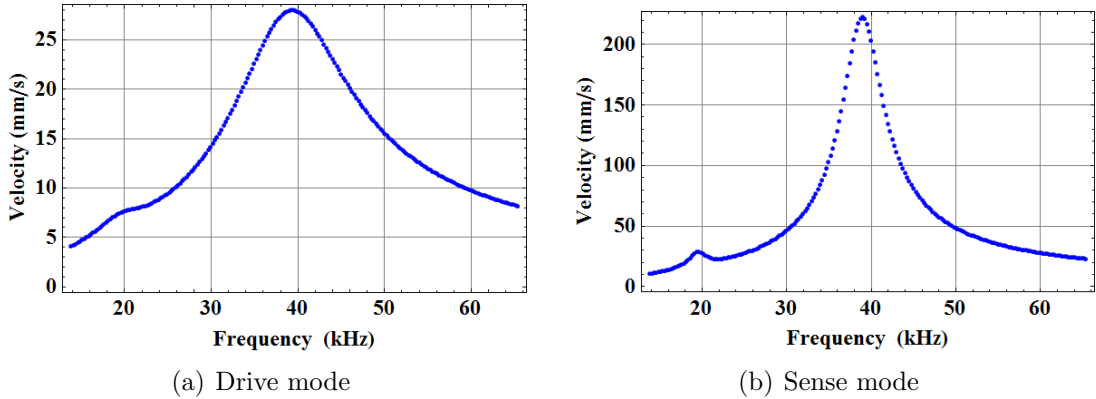


Figure 2.4: The frequency-response curves of the drive and sense modes for the PolyMUMPs gyroscope

Assuming low damping, to better capture the natural frequency of the gyroscope, the model quality factor was set to  $Q = 100$ . The relationship

$$c_i = \frac{\sqrt{k_i m}}{Q} \quad (2.3)$$

was used to substitute for the damping coefficients appearing in Eqs. (2.1) and (2.2). For the excitation signal of  $V_d = 5 + 3 \cos(\omega t)$  V, the drive mode equation of motion, Eq. (2.1), was integrated numerically for long time, 600 excitation cycles or  $1200\pi/\omega$ , until the response settled down to steady-state. The frequency-response curve of the PolyMUMPs gyroscope drive mode, Figure 2.4(a), was obtained by calculating the peak-to-peak velocity of the micro-plate center over the last 300 excitation periods ( $600\pi/\omega$ ) as the frequency was varied over the range [15:82] kHz. The same procedure was followed to obtain the frequency-response curve of the sense mode, Figure 2.4(b), where the excitation signal was set to  $V_s = 30 + 10 \cos(\omega t)$  V and the frequency range to [250-850] kHz. The natural frequency of the drive mode is approximately equal to the peak of its frequency response  $f_d = 40$  kHz. Similarly, the natural frequency of the sense mode was found to be approximately  $f_s = 41$  kHz. Figure 2.5(a) shows the relationship between the microplate's center out-of-plane (drive) deflection and the dc voltage of the bottom electrode for the SOIMUMPs gyroscope. Similarly, Figure 2.5(b) shows the in-plane (sense) deflection as a function of a side electrode dc voltage. In both cases, the deflection increases with voltage until the pull-in point. The pull-in voltage was calculated as 19V for the out-of-plane direction and 49V for the in-plane direction.

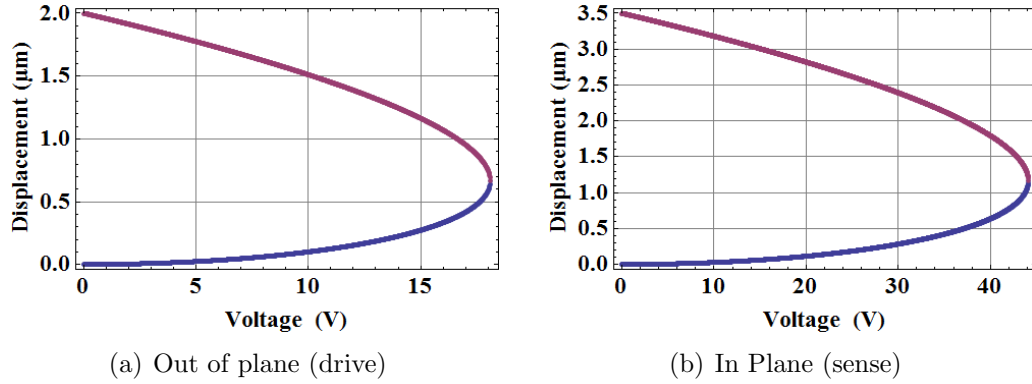


Figure 2.5: The displacement-voltage relationship for the SOIMUMPs gyroscope

Following a similar procedure to that described above, the frequency-response curve of the SOIMUMPs gyroscope in the drive direction was obtained for the excitation signal  $V_d = 5 + 3 \cos(\omega t)$  V in the frequency range of [5:20] kHz. It is shown in Figure. 2.6(a) where the peak response, corresponding approximately to the natural frequency, occurs at  $f_d = 40$  kHz. The frequency-response curve of the sense mode is shown in Figure. 2.6(b) for the excitation signal  $V_s = 5 + 3 \cos(\omega t)$  V and the frequency range [20-100] kHz. The natural frequency of the sense mode occurs approximately at the peak of the frequency-response curve calculated as  $f_s = 42.5$  kHz.

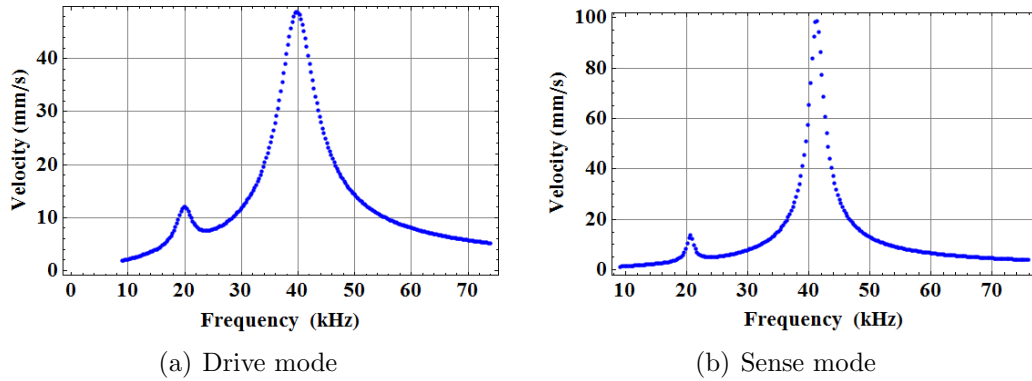


Figure 2.6: The frequency-response curves of the drive and sense modes for the SOIMUMPs gyroscope



## 2.4 Modal Analysis

Finite Element Analysis (FEA) is a numerical technique for finding approximate solutions of partial differential equations (PDE). The solution approach is based either on eliminating the differential equation completely (static analysis), or rendering the PDE into an approximating system of ordinary differential equations, which are then numerically integrated using standard techniques such as Euler’s method, Runge-Kutta, etc. Simulations of the gyroscopes were performed with COMSOL software package [62].

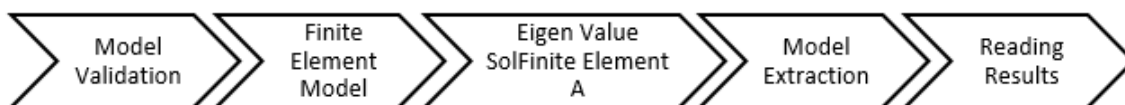


Figure 2.7: Block diagram of ANSYS Modal Analysis solution

Modal analysis is the study of structural mode shapes and natural characteristics [62]. Figure 2.7 shows the process flow for modal analysis in COMSOL. At this first stage, COMSOL checks the validity of the model geometry, in addition to defining Young’s modulus and material density. The second stage is element meshing, where an infinite dimensional volume is reduced to a finite number of nodes connected to form elements. In our case, a fine mesh size was used throughout the structure.

To solve a system of  $N$  nodes, a  $(3N \times 3N)$  matrix is created where each of the three nodal displacements is treated as an unknown. The Eigenvalue solver converts coupled system equations into an uncoupled system of equations that is algebraically manipulated (solved) to obtain the mode shapes. Next, mode shapes are extracted. For a Finite Element Model (FEM) of  $N$  DOF, at least  $N$  mode shapes and resonant frequencies can be extracted.

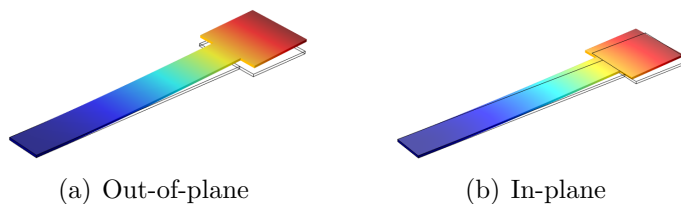


Figure 2.8: The first out-of-plane and in-plane bending modes of the PolyMUMPs gyroscope

Finally, the modal analysis results can be read in the result tree, where the modes are listed. At each mode, shape deformation can be plotted, in which an arbitrary force is applied to observe the full-scale dynamic behavior. For the PolyMUMPs gyroscope, the natural frequencies of the first out-of-plane and in-plane bending modes were found to be 30 kHz and 115 kHz, respectively. The corresponding mode shapes are shown in figure 2.8 (a) and (b), respectively. For the SOIMUMPs gyroscope, the first out-of-plane and in-plane natural frequencies were found to be 43 kHz and 45 kHz. The corresponding mode shapes are shown in Figure 2.9, respectively. The natural frequencies of the two gyroscopes are listed in Table 2.2. Comparing these values to those obtained from the numerical simulation of the frequency-response curves in section 2.3, we find that the drive and sense modes natural frequencies are close for both the lumped mass model and the FEM simulations.

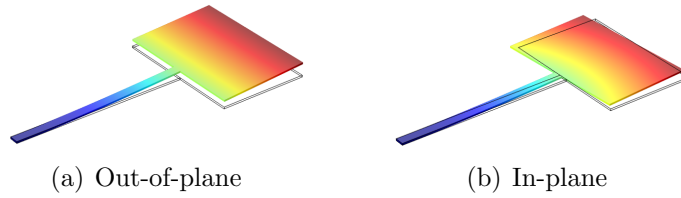


Figure 2.9: The first out-of-plane and in-plane bending modes of the SOIMUMPs gyroscope

Table 2.2: Simulated natural frequencies for the drive and sense modes.

Mode	PolyMUMPs	SOIMUMPs
Drive mode (kHz)	30	43
Sense mode (kHz)	115	45

As can be seen, for the PolyMUMPs design, the FEA simulated drive mode frequency (30 kHz) was sufficiently close to the one obtained from the lumped mass model (40 kHz). However, the FEA simulated sense mode was nearly 115 kHz compared to the calculated value at 41 kHz, indicating a degree of frequency mismatch between the drive and sense mode. For the SOIMUMPs case, the FEA simulated drive and sense mode natural frequencies were close to those obtained from the lumped model at 43 kHz compared to 40 kHz and 45 kHz compared to 42.5 kHz, respectively.

# Chapter 3

## Gyroscope Fabrication

This chapter presents the steps of the MVGs fabrication processes. Cantilever beam gyroscope were fabricated using a bulk micromachining process (SOIMUMPs) and a surface micromachining process (PolyMUMPs). The developed gyroscopes serve as a testbed for new sense methods and novel design approaches. Section 3.1 presents the standard Silicon-On-Insulator (SOI) fabrication process offered by MEMSCAP. Section 3.2 details the post-processing of SOIMUMPs gyroscopes carried out at the Quantum Nanofab Centre (QNC). Lastly, section 3.3 elaborates on PolyMUMPs fabrication process also offered by MEMSCAP.

### 3.1 SOIMUMPs Gyroscopes

SOIMUMPs, Silicon-On-Insulator-Multi-User-MEMS-Processes, is a bulk micromachining process that uses Deep Reactive Ion Etching (DRIE) on Silicon-On-Insulator (SOI) wafers in order to pattern features such as beams. The standard crystal silicon thicknesses offered are 10  $\mu\text{m}$  and 25  $\mu\text{m}$ , whereas the minimum feature size allowed is 2  $\mu\text{m}$ . Our devices were fabricated in a structural silicon layer thickness of 25  $\mu\text{m}$  [61].

#### 3.1.1 Manufacturing Layout

Figure 3.1 shows a detailed layout of the gyroscope elements drawn in L-Edit. The device elements are defined in Table 3.1.

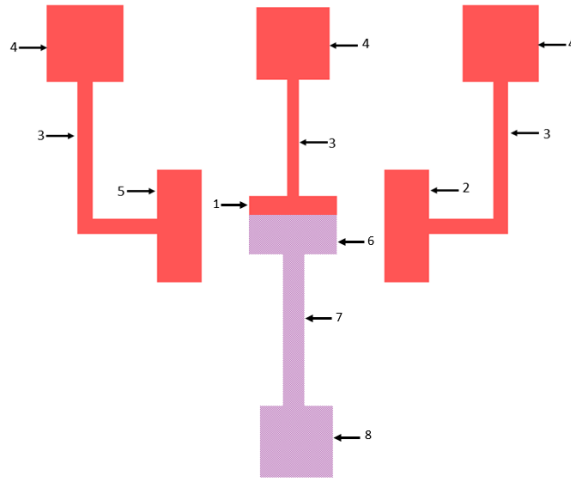


Figure 3.1: A snapshot of the overall L-Edit layout

Table 3.1: Elements of the SOIMUMPs gyroscope

Component	Description
1	Bottom (drive) electrode
2	Right sense electrode
3	Electrical connections
4	Electrode contact pads
5	Left sense electrode
6	Micro-plate
7	Cantilever beam
8	Beam contact pad

The drive electrode (1) is patterned under the micro-plate (6). A cantilever beam (7) supports the micro-plate. Three gold pads (4) provide electric contact to the side and bottom electrodes. Another contact pad (8) provides electric contact to the cantilever

beam. Gold metalization lines (3), blanket-metal substrates, connect the contact pad to the electrodes. The sense electrodes (2 & 5) serve as a reference for capacitance measurement.

### 3.1.2 Process Flow

The fabrication process uses a two-mask process flow. Figure 3.2 illustrates the fabrication steps. The process starts with cleaning of the SOI wafers to remove organic and inorganic residues followed by wet oxidation of the wafer to develop 1.6  $\mu\text{m}$  of silicon dioxide ( $\text{SiO}_2$ ) on the crystalline side of the wafer. The first mask (Mask 1) defines the DRIE trenches and pad areas by patterning a phototresist (PR) layer spun on the SOI wafer. After PR patterning, the uncovered  $\text{SiO}_2$  is etched in the DRIE using special recipe for  $\text{SiO}_2$  etching.

	Cross-section	3D model	Description
a			silicon dioxide layer is deposited on top of the device layer using plasma-enhanced chemical vapordeposition (PECVD). a thicker photo resistis (PR) deposited.
b			PR patterned on top of the silicon dioxide layer. RIE is used to etch silicon dioxide layer.
c			The structure of bulk sidewall electrodes is obtained by deep reactive ion etching (DRIE).
d			Au layers are sputtered on the sidewall surface using the CVC Sputter Deposition System.
e			The electrode layer (Au) is patterned to create the connection circuit and side wall electrodes.

Figure 3.2: SOIMUMPs Process Flow

The wafers are bulk etched using the Bosch process in the DRIE machine to remove uncovered areas of crystalline silicon. Metal pads are formed by sputtering gold (Au)

on the wafer, followed by patterning the second PR layer using Mask 2, and finally wet etching of the uncovered Au regions. The resulting wafer has the bottom electrode, side electrodes and electrical connections among them and their contact pads. The gyroscope structural elements, cantilever beam and micro-plate, are yet to be fabricated.

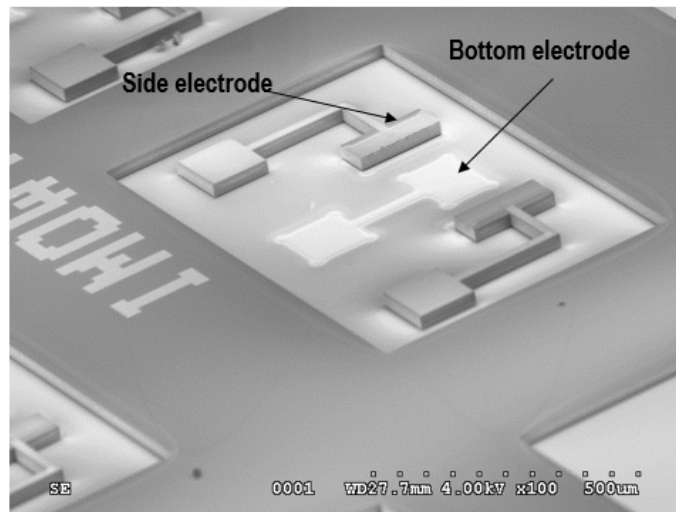


Figure 3.3: SEM picture of the ‘as-received’ SOIMUMPs die

## 3.2 Post-processing of SOIMUMPs

This section presents the post fabrication process implemented at the Quantum Nanofab Centre (QNC), University of Waterloo. The SEM image of the ‘as received’ SOIMUMPs die, Figure 3.3, shows the two side electrodes, the bottom electrode and the electrical connection. The dies were subject to back-to-front processes at QNC to deposit the missing structures. Accomplishing these fabrication step was challenging since it had to be carried out manually die-by-die, with die dimensions of 4.75 mm x 4.75 mm.

### 3.2.1 Height Measurement

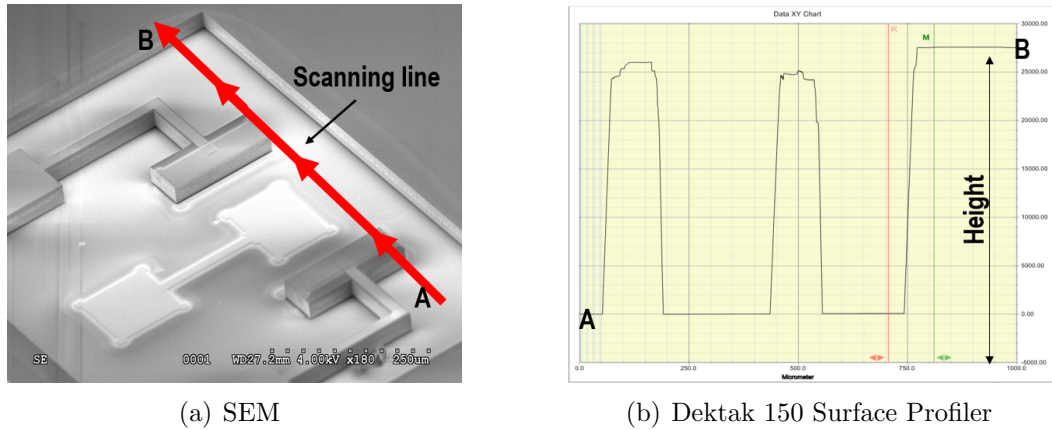


Figure 3.4: Height measurements by used Dektak 150 Surface Profiler

Upon receiving the SOIMUMPs dies, we measured the height of each structure using the Dektak 150 Surface Profilometer, along the A-B line shown in Figure 3.4 (a). The height of the two side electrode measured from the profile, Figure 3.4 (b), we found to be  $25\ \mu\text{m}$ . The side and bottom electrodes were deposited on the substrate surface inside a  $27\ \mu\text{m}$  cavity. Figure 3.5 shows a schematic of the device cross section.

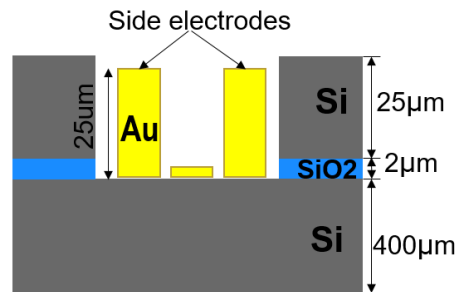


Figure 3.5: Cross sectional view showing all layers

### 3.2.2 Silicon Etching

In this step, we etched the outer region surrounding the electrodes area in preparation for deposition of the micro beam and its anchor in that space. First, the electrodes were protected by depositing a layer of photoresist and spin-coating. Selective deposition to the electrode area only was possible without the use a mask by taking advantage of the cavity depth and using a special recipe for spin coating that resulted in removing the photoresist everywhere else, Figure 3.6 (b).

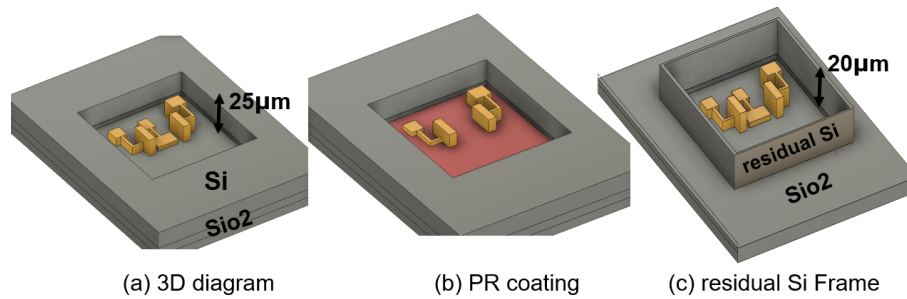


Figure 3.6: DRIE Etching of the Silicon

After that, the unprotected 25 μm layer of crystalline Si was bulk-etched using the Bosch process in the DRIE machine. Figure 3.6 (c) shows the result of the process. A residual 20 μm high wall was left surrounding the electrode area.

### 3.2.3 Die Cleaning

A further cleaning step was required to remove the PR and the residual silicon walls from the die. We used an O<sub>2</sub> plasma asher to remove the organic material (PR) and turn the inorganic material (residual Si) to ash. Figure 3.7 (a) shows a schematic of the die before and after using the plasma asher. SEM picture of the process result appears in Figure 3.7 (b). Most of the PR was removed as well as sections of the residual walls. The remaining wall sections had a much lower height.



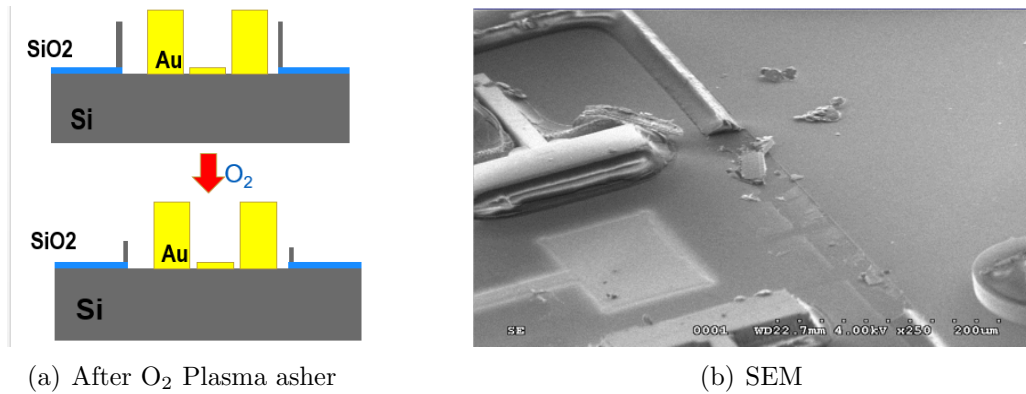


Figure 3.7: (a) A schematic of the cross-sectional view before and after plasma ashing and (b) SEM picture of the die after plasma ashing

To remove the remaining PR and wall sections, Piranha cleaning was carried out. The sample was immersed in a solution of hydrogen peroxide  $H_2O_2$  and sulfuric acid  $H_2SO_4$ , which reacted with and removed the PR and the silicon wall residuals. A schematic and SEM picture of the result are shown in Figure 3.8.

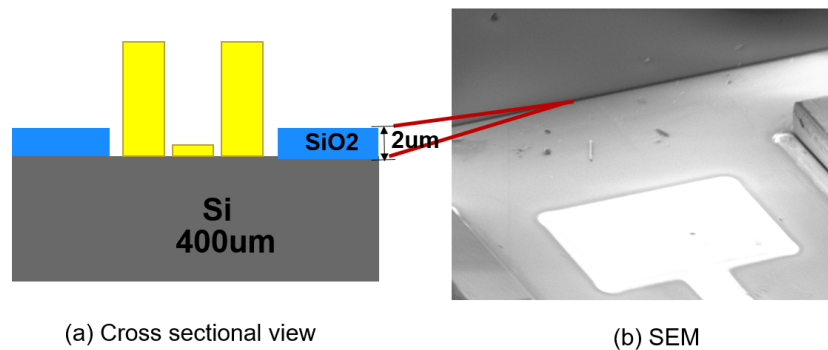


Figure 3.8: (a) A schematic cross-sectional view and (b) SEM picture of the die after removing residual Si walls using Piranha cleaning

### 3.2.4 Wet Etching of Silicon Dioxide

The last step in surface preparation is the removal of the  $SiO_2$  stop layer using by wet Buffered Oxide Etch (BOE). The goal of this step is substrate surface planarization. A

mixture of a buffering agent and ammonium fluoride ( $\text{NH}_4\text{F}$ ) and HF was used to achieve omni-directional  $\text{SiO}_2$  etch. A schematic of the die before and after wet etching is shown in Figure 3.9 (a). The SEM picture of the result is shown in Figure 3.9 (b).

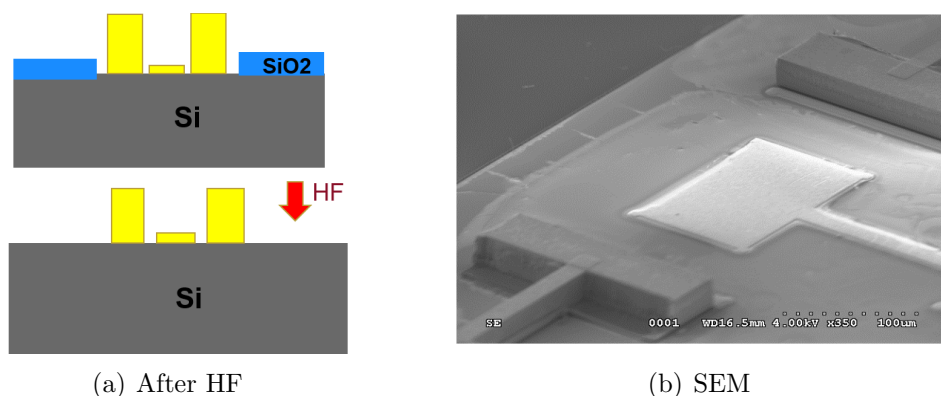


Figure 3.9: (a) Schematic of the die before and after buffered oxide etch of  $\text{SiO}_2$  and (b) SEM picture of the result

### 3.2.5 Silicon Dioxide Deposition

We deposited  $2 \mu\text{m}$  of sacrificial  $\text{SiO}_2$  using Plasma Enhanced Chemical Vapor Deposition (PECVD) on top of the substrate. A schematic of the die after  $\text{SiO}_2$  deposition is shown in Figure 3.10 (a). The corresponding SEM picture of the die is shown in Figure 3.10 (b). All surfaces of the die are covered in  $\text{SiO}_2$  including the side electrodes.

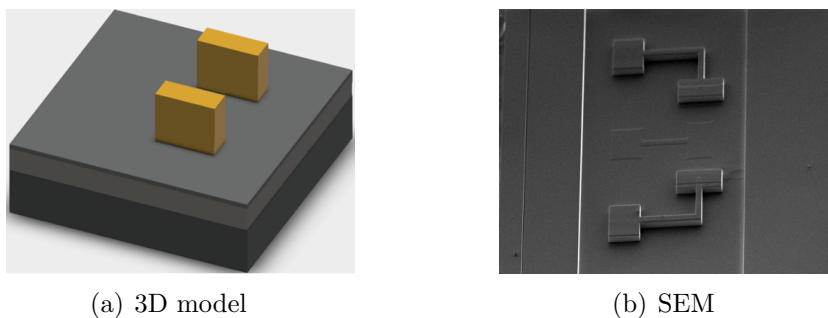


Figure 3.10: (a) Schematic and (b) SEM picture of the die after PECVD of  $\text{SiO}_2$

### 3.2.6 Photolithography

Lithography is a process that uses UV light to transfer a pattern from a mask to a photosensitive layer. Figure 3.11 shows the step of the lithography process. First a small amount of PR is deposited in the middle the die, using a micro pipette, spin coated over the die surface using the special recipe for small die. After that, mask aligner MA6 is used to expose the die to UV light through Mask 1 and transfer the pattern of the anchor to the PR layer. Subsequently, the die was immerses into the developer to remove unexposed PR.

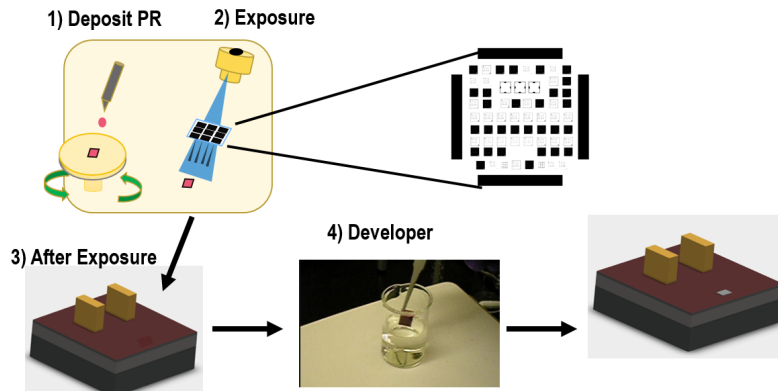


Figure 3.11: Lithography process

### 3.2.7 Dry Etching of Silicon Dioxide

The uncovered  $\text{SiO}_2$  region is etched using the standard recipe for Reactive Ion Etching (RIE). Figure 3.12 (a) shows a schematic of the die before and after  $\text{SiO}_2$  dry etching. The SEM picture, Figure 3.12(b), shows the exposed anchor area.

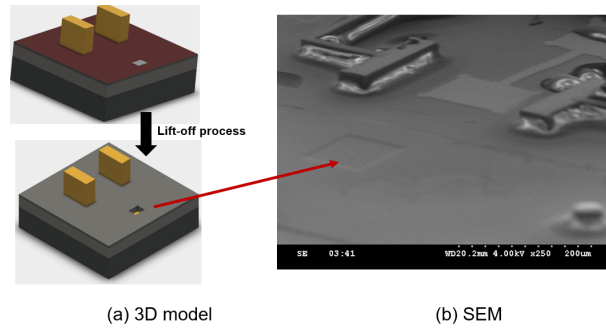


Figure 3.12: SiO<sub>2</sub> etching using RIE

### 3.2.8 Structural Layer Deposition

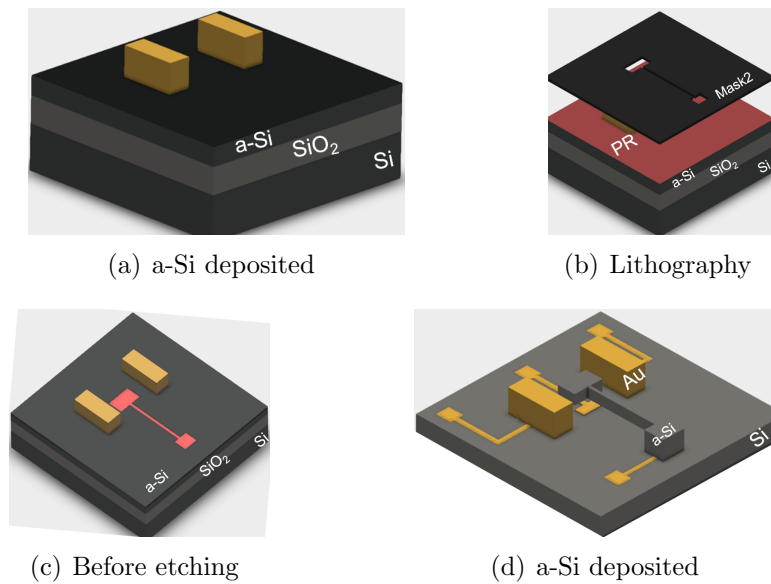


Figure 3.13: Deposition and patterning of the gyroscope structure

Following a similar procedure to that described in subsections 3.2.5 and 3.2.6, the gyroscope structure was deposited and patterned. First, 2  $\mu\text{m}$  of amorphous silicon (a-Si) was deposited on top of the SiO<sub>2</sub> layer, Figure 3.13 (a). Subsequently, Mask 2 was used to pattern the support beam, micro-plate and anchor to the a-Si layer, Figures 3.13 (b) and

(c). After that, the unprotected a-Si layer was bulk-etched using the Bosch process in the DRIE machine. Next, unexposed a-Si was removed using RIE. Finally, the SiO<sub>2</sub> layer was removed in order to release the gyroscope structure using a wet etching (HF) similar procedure to that described in 3.2.4. A schematic of the released gyroscope is depicted in Figure 3.13 (d). The post-processing steps of SOIMUMPs gyroscopes are summarized in the table shown in Figure 3.14.

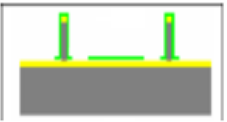
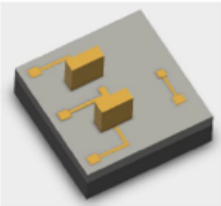

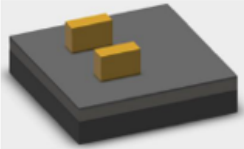
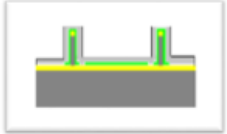
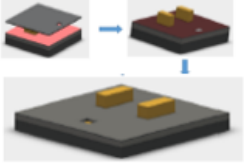



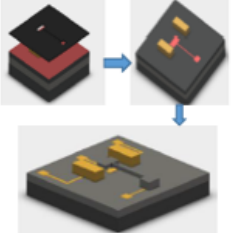
	Cross section	3D model
a		
b		
c		
d		
e		

Figure 3.14: Process flow for post processing of SOIMUMPs dies

### 3.3 PolyMUMPs Gyroscope

PolyMUMPs process has 7 layers, 3 polysilicon layers serve as structural and electrode layers, 2 levels of phosphosilicate glass (PSG) as sacrificial layers, 1 layer of silicon nitride is used for electrical insulation, and 1 gold metallization layer. Figure 3.15 provides an overview of the PolyMUMPs process layers and fabrication steps used in the fabrication of the PolyMUMPs gyroscope.


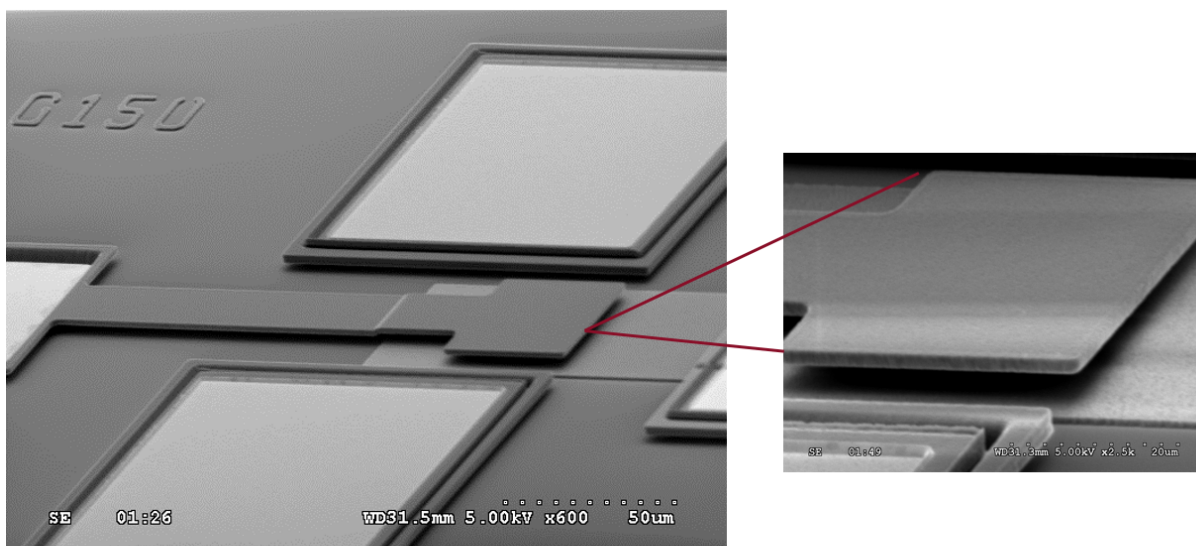
NO.	Cross-section	Description
1		Starting with (100) silicon wafers of
2		Deposit passivation Layer silicon nitride as an electrical isolation layer
3		Poly0 deposition 500nm (LPCVD) to create bottom electrodes
4		Pattern the Structural Layer Poly 0 by RIE
5		Deposit 2 μm phosphosilicate glass (PSG) sacrificial layer 1 deposited by LPCVD
6		RIE etch of PSG1 to create the anchor
7		the first structural layer of polysilicon (Poly 1) is deposited at a thickness of 2 μm by LPCVD
8		Gold Metallisation by Lift Off 0,5μm (METAL)
9		Structure release by wet etching : HF 49% (1.5 to 2 mn)

Figure 3.15: PolyMUMPs gyroscope fabrication steps

First, a 100 silicon wafer is prepared and used as a device substrate. Secondly, a

silicon nitride ( $\text{Si}_3\text{N}_4$ ) layer is deposited on top of the substrate using Chemical Vapor Deposition (CVD).  $\text{Si}_3\text{N}_4$  acts as an electrical insulation. Following this, a 500 nm thick polysilicon layer (Poly0) is conformally deposited using LPCVD. Poly0 is then patterned and reactively ion etched in order to create substrate electrodes. Next, a first sacrificial of 2 $\mu$  phosphosilicate glass (PSG) is deposited by LPCVD. The first PSG layer is patterned and selectively etched to define the gyroscope anchor. Using LPCVD once again, the second polysilicon layer (Poly1) is deposited at a 2  $\mu\text{m}$  thickness. Then, a 0.5  $\mu\text{m}$  thick gold is deposited on the substrate electrode using a lift-off process. Finally, the first PSG layer is removed by HF wet etching. Figure 3.16 shows SEM pictures of the PolyMUMPs fabricated gyroscope [65].



(a) SEM of PolyMUMPs

(b) SEM of PolyMUMPs

Figure 3.16: SEM pictures of the PolyMUMPs gyroscope

# Chapter 4

## Test and Characterization

### 4.1 Optical Detection

Optical detection methods were used to characterize the fabricated gyroscopes and to obtain their frequency response. The experimental setup is shown in Figure 4.1. The function generator, appearing in the left panel of the figure, was used to supply the excitation signal to the drive or detection electrode. Ploytec MSV-400 vibrometer, shown in the center panel of the figure, was used to measure the vibrations of the micro-plate. The chip carrier containing the die, left panel of the figure, is placed on the probe station chuck under the vibrometer objective lens. The vibrometer focuses a laser beam on a point on the micro-plate to measure its out-of-plane velocity and displacement.

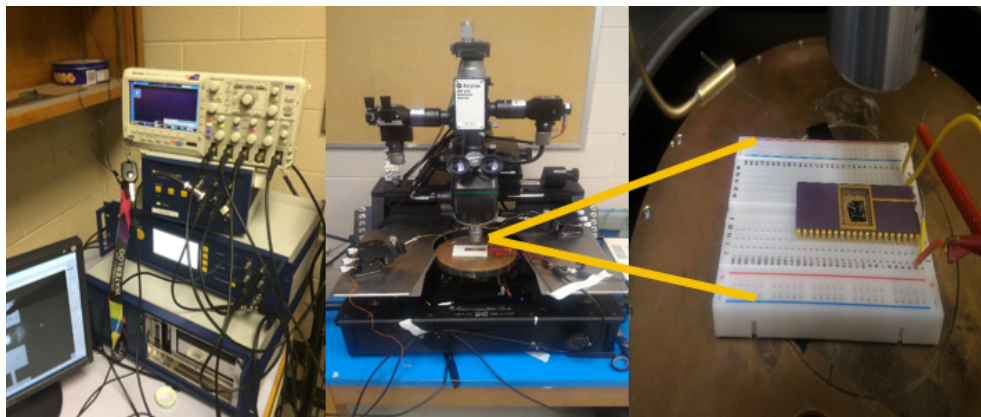


Figure 4.1: Experimental Setup



Laser-Doppler-Vibrometry (LDV) is a non-contact motion measurement technique based upon the Doppler shift Effect. When a coherent laser light is reflected from the surface of a moving object, a Doppler shift (DS) occurs in the frequency of the reflected laser beam proportional to the surface velocity component aligned with the beam propagation direction. Measuring the shift in the frequency and phase of the reflected laser beam allows for the detection of the object’s velocity and displacement, respectively

## 4.2 Characterization of Drive Mode

We measured the frequency-response curve of the PolyMUMPs gyroscope drive mode, Figure 4.2 (a), in air by applying a pulse train with an amplitude of 10 V, a frequency of 1 kHz, and an 8% duty cycle to the bottom electrode as shown schematically in Figure 4.2 (b). The laser beam was focused on the micro-plate center point to measure its out-of-plane velocity (drive mode). The Polytec Scanning Vibrometer (PSV) software interface was used to generate the frequency-response curve shown in the top panel of Figure 4.3 while the time-domain response is shown in the bottom panel.

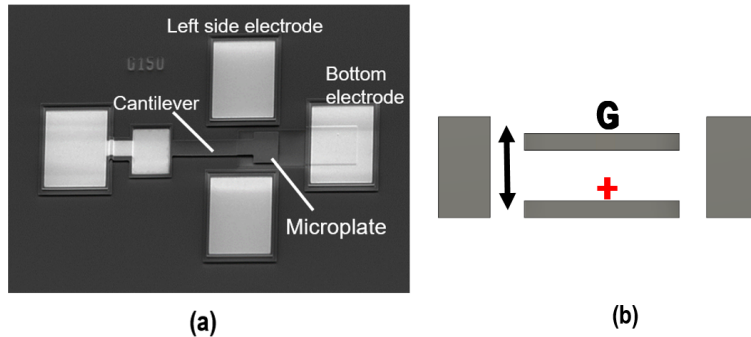


Figure 4.2: (a) SEM of the PolyMUMPs gyroscope. (b) Schematic diagram of drive mode actuation

The damped natural frequency of the gyroscope was measured from the curve as  $\bar{f}_d = 40$  kHz. The quality factor was also calculated from the curve using the half-power bandwidth method as  $Q = 1$ . The time-domain response, Figure 4.3, shows a single oscillation in response to the excitation pulse before the micro-plate settled down to equilibrium, thereby confirming our estimate of the quality factor.

Substituting the values for the damped natural frequency and the quality factor in Eq. (1.17), we can calculate the (undamped) natural frequency of the drive mode as  $f_d =$

46.2 kHz. This value compares closely with those obtained from the lumped mass model (40 kHz) and FEM simulations (30 kHz). Apparently, the experimental natural frequency drifted due to fabrication under-etching or over-etching. These imperfections were neither input in the lumped mass model nor simulated in the COMSOL FEA solution.

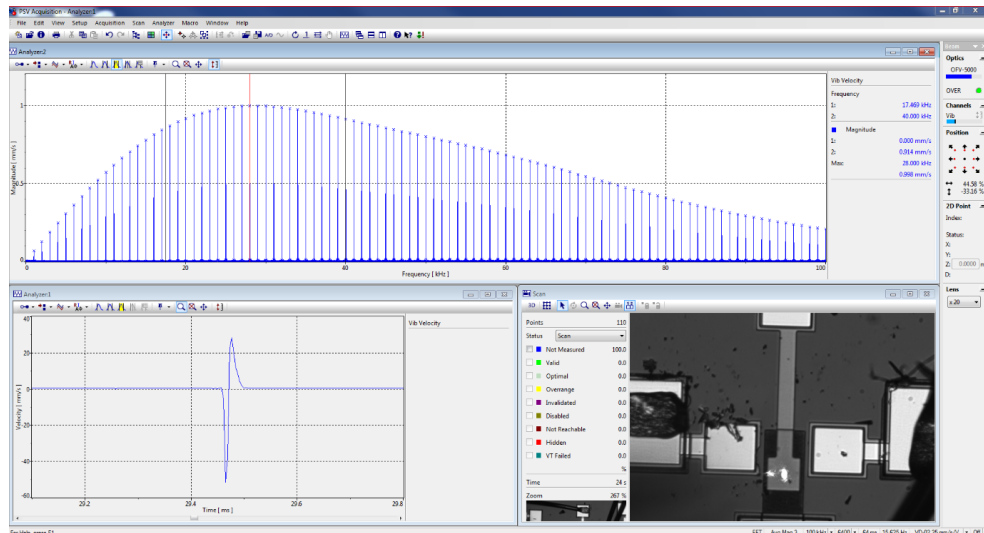


Figure 4.3: A screen capture of the laser vibrometer interface showing the frequency-response (top panel) and the time-domain response (bottom panel) of the drive mode velocity under a pulse train excitation

### 4.2.1 Pull-in Voltage

Exciting the gyroscope with a voltage signal much smaller than its natural frequency results in quasi-static response, where the micro-plate distance from the actuation electrode is controlled by the electrostatic force in the absence of dynamic amplification. This actuation mode can be used to measure the gyroscope static response and its static pull-in voltage. At this voltage, the microplate collapses onto the actuation electrode.

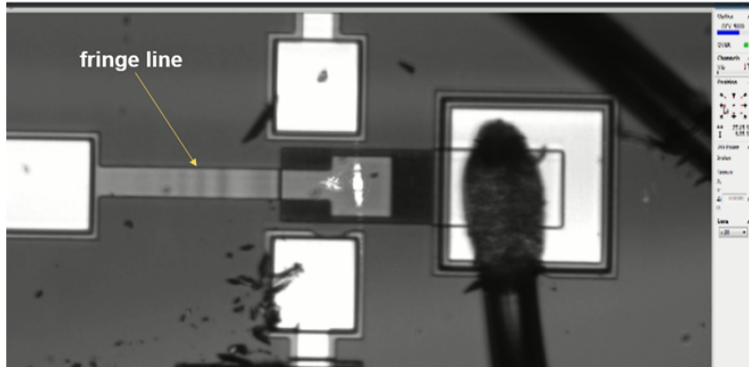


Figure 4.4: Pull in voltage

In order to determine the pull-in voltage of the drive mode, a harmonic signal was applied to the bottom electrode pad as shown in Figure 4.2 (b). The frequency of the signal was set to  $f = 2$  Hz, faraway from the drive mode natural frequency. As the microplate moved in the out-of-plane direction, its image in the video microscope appeared to blur as it moved into and out-of-focus. When pull-in occurred, this motion pattern stopped.

The maximum voltage of the waveform was monotonically increased until pull-in was observed in this fashion at  $V_{Pi} = 18$  V. Pull-in was verified optically by the formation of alternating bright and dark fringe lines along the beam length as shown in Figure 4.4 in the absence of actuation voltage. This indicated that the beam was bent down toward the bottom electrode a distance larger than quarter of light wavelength resulting in those fringe lines.

### 4.3 Characterization of Sense Mode

In-plane mode oscillations (with reference to our device) are not observable under the vibrometer since they do not involve an out-of-plane component. To overcome this challenge, the chip carrier was first placed on a tilt stage as shown in Figure 4.5. As a result, motions in the plane of the gyroscope developed an out-of-plane component with respect to the incident laser beam.

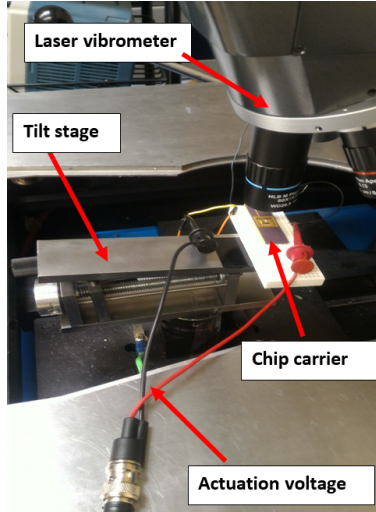


Figure 4.5: The chip carrier placed on the tilt stage

Setting the stage tilt angle to  $10^\circ$  with respect to the horizontal plane, we measured the frequency-response curve of the PolyMUMPs gyroscope, Figure 4.6 (a), sense mode in air by applying a pulse train with an amplitude of 10 V, a frequency of 1 kHz, and an 8% duty cycle to one of the side electrode as shown schematically in Figure 4.6 (b). The laser beam was focused on a point at the micro-plate edge to measure the out-of-plane component of the sense mode velocity. The interface PSV generated the frequency-response curve, Figure 4.7. The frequency-response is shown in the top panel of Figure 4.7 while the time-domain response is shown in the bottom left panel. The actuated electrode is marked with a ‘+’ in the picture appearing in the bottom right panel of the figure while the laser focus point appears as a shiny spot in the picture.

The damped natural frequency was measured from the curve in Figure 4.7 as  $\bar{f}_s = 55$  kHz. The quality factor was calculated from the same curve using the half-power bandwidth method as  $Q = 1$ . Using Eq. (1.17), we calculated the natural frequency of the sense mode as  $f_s = 55.5$  kHz, which is about 15 kHz higher than that of the lumped mass model natural frequency (41 kHz).

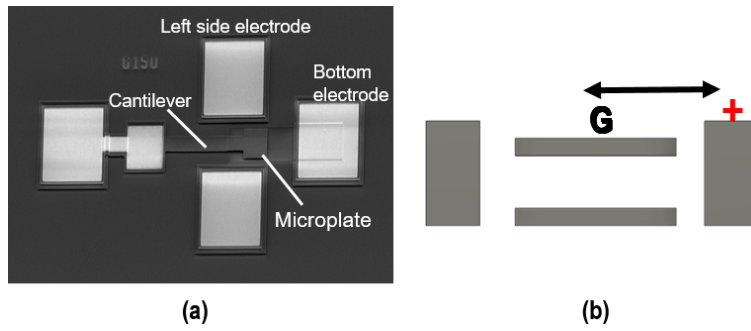


Figure 4.6: (a) SEM of the PolyMUMPs gyroscope. (b) Schematic diagram of sense mode actuation

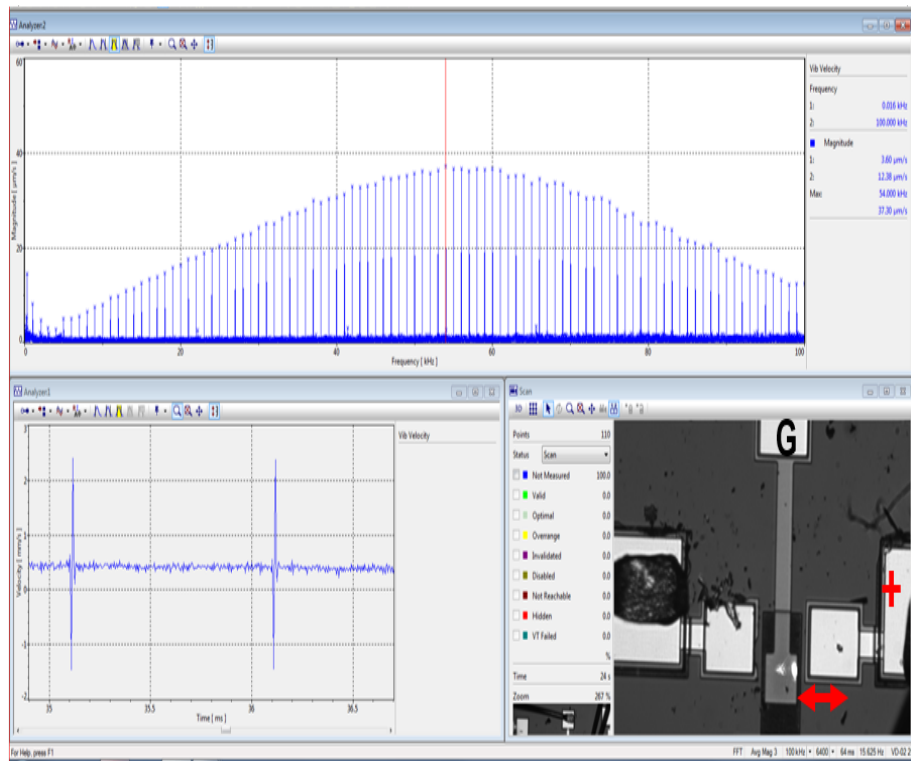


Figure 4.7: A screen capture of the laser vibrometer interface showing the frequency-response (top panel) and the time-domain response (bottom panel) of the sense mode velocity under a pulse train excitation

The pull-in voltage of the sense mode was not measured since the optical method described in subsection 4.2.1 was not applicable to in-plane motions. On the other hand, it was observed that pull-in towards the bottom electrode occurred as the dc voltage applied to one of the side electrodes exceeded  $V_s = 75$  V. This secondary pull-in is evidence of capacitive coupling between the side electrodes and the bottom electrode.

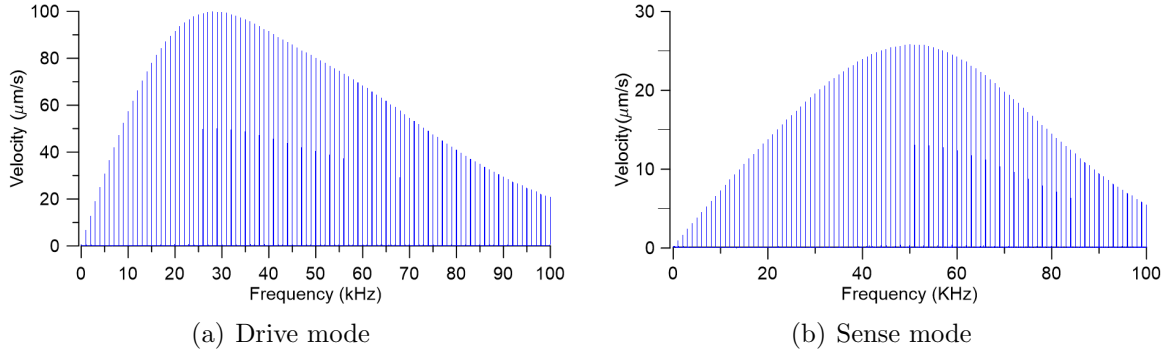


Figure 4.8: Plots of the (a) drive and (a) sense modes frequency response under a pulse train

Comparing the drive mode and sense mode frequency responses, depicted in figure 4.8, we found that the drive-mode maximum velocity was fourfold the out-of-plane component of the sense-mode velocity at  $100 \mu\text{m/s}$  compared to  $25 \mu\text{m/s}$ . Using the tilt angle, we calculated the maximum in-plane velocity as  $144 \mu\text{m/s}$ . This corresponds well with the ratio of the damped natural frequency of the sense to the drive mode at 1.375, indicating that the response size in both directions is similar.

# Chapter 5

## Conclusions and Future Work

### 5.1 Conclusions

Over the course of this research project, we designed, fabricated and tested two MEMS vibratory gyroscopes. The two design portfolios can serve as a stepping stone to target potential gyroscope applications. Further, the availability of unpackaged gyroscopes that can be characterized optically, as well as the traditional electrical characterization methods, is an important result. It will allow the use of these gyroscopes as a testbed to investigate new operational modes and actuation schemes.

Two classes of cantilever beam gyroscope were fabricated. The first used SOIMUMPs to fabricate the side and bottom electrodes. The second class was fabricated completely using the PolyMUMPs process. The fabrication of the SOIMUMPs gyroscopes was completed at QNC, where the gyroscope anchor, cantilever beam and micro-plate were deposited using a back-to-front approach. However, the gyroscope was not completely released due to the unavailability of a Critical Point Dryer at QNC. As a result, we were not able to characterize it.

It is worth noting that while the initial plan was to fabricate the cantilever beams of the SOIMUMPs gyroscopes with a thickness of  $10\ \mu\text{m}$ , I was able only to achieve a maximum thickness of  $2\ \mu\text{m}$  due to the limitations of the PECVD process. Therefore, SOIMUMPs gyroscopes were redesigned with a structural layer thickness of  $2\ \mu\text{m}$  to achieve target resonance frequency of 48.6 kHz and 49 kHz for the drive and sense modes, respectively. On the other hand, a  $2\ \mu\text{m}$  structural thickness is a standard option the PolyMUMPs, which allowed us to use the standard process as-is.

We characterized the PolyMUMPs gyroscopes using LDV optical measurements. This optical method provided very accurate measurements for the drive mode motion. However, in the case of the sense mode, a tilt stage was used in order to allow the LDV to measure its in-plane motion, which led to an indirect measurement. Experimentally, we measured the drive and sense mode frequency at 46.2 kHz and 55.5 kHz, respectively; the sense mode was a few kHz higher than that of the drive mode. These experimental values were different from the calculated drive and sense mode natural frequencies: 40 and 41 kHz, respectively.

## 5.2 Future Work

It is not uncommon for a MEMS gyroscope to undergo multiple design iterations. Characterization of our gyroscopes has delineated those issues that require addressing the next design cycle.

First, it is necessary to use the Critical Point Dryer to release the fabricated SOIMUMPs gyroscopes. Further, they should be characterized along similar lines to their PolyMUMPs counterparts and the results compared. Second, we suggest use the MicraGEM fabrication process to achieve a gyroscope with a structural layer thickness of 10  $\mu\text{m}$  and, therefore, a larger inertial mass.

Third, we should have in possession a full-field ( $360^\circ$ ) LDV capable of in-plane and out-of-plane measurements. This would provide us further accurate in-plane cantilever measurements.

Finally, in order to test the overall performance of our gyroscopes, we propose a single-port frequency-modulated excitation and detection scheme in order to measure their sensitivity and characterize their performance. Both vacuum packaged and glass packaged samples should be tested.



# Bibliography

- [1] Acar, C., and Shkel, A. (2008). MEMS vibratory gyroscopes: structural approaches to improve robustness. Springer Science and Business Media.
- [2] Gyroscope. Available
- [3] Hilkert. (Feb 2008). Inertially Stabilized Platform Technology. IEEE Control Systems Magazine. p26-29.
- [4] Kaajakari (2009). Practical MEMS. Las Vegas: Small Gear Publishing
- [5] Miller, Cowen, et al (2004). SOIMUMPS Design Handbook. 4th ed. USA: MENScaP. p1-8.
- [6] Sderkvist, J. (1994). Micromachined gyroscopes. Sensors and Actuators A: Physical, 43(1-3), 65-71.
- [7] Yazdi, N., Ayazi, F., and Najafi, K. (1998). Micromachined inertial sensors. Proceedings of the IEEE, 86(8), 1640-1659.
- [8] Shkel, A. M. (2001, August). Micromachined gyroscopes: challenges, design solutions, and opportunities. In SPIE's 8th Annual International Symposium on Smart Structures and Materials (pp. 74-85). International Society for Optics and Photonics.
- [9] Xie, H., and Fedder, G. K. (2003). Integrated microelectromechanical gyroscopes. Journal of aerospace engineering, 16(2), 65-75.
- [10] Weinberg, M. S., and Kourepenis, A. (2006). Error sources in in-plane silicon tuning-fork MEMS gyroscopes. Journal of Microelectromechanical systems, 15(3), 479-491.

- [11] Lee, B. L., Lee, S. W., Jung, K. D., Choi, J. H., Chung, T. R., and Cho, Y. C. (2001). A de-coupled vibratory gyroscope using a mixed micro-machining technology. In *Robotics and Automation, 2001. Proceedings 2001 ICRA. IEEE International Conference on* (Vol. 4, pp. 3412-3416). IEEE.
- [12] Bernstein, J., Cho, S., King, A. T., Kourepenis, A., Maciel, P., & Weinberg, M. (1993, February). A micromachined comb-drive tuning fork rate gyroscope. In *Micro Electro Mechanical Systems, 1993, MEMS'93, Proceedings An Investigation of Micro Structures, Sensors, Actuators, Machines and Systems. IEEE.* (pp. 143-148). IEEE.
- [13] Wu, H. (2009). System architecture for mode-matching a MEMS gyroscope (Doctoral dissertation, Massachusetts Institute of Technology).
- [14] Sujatha, L., & Preethi, B. Design and Analysis of MEMS Gyroscope.
- [15] Trusov, A. A. (2011). Overview of MEMS gyroscopes: history, principles of operations, types of measurements. University of California, Irvine, USA, maj.
- [16] Ayman Alneamy (2016). Combined Electrostatic/Electromagnetic MEMS Actuators. UWSpace. <http://hdl.handle.net/10012/10622>
- [17] Hashimoto, M., Cabuz, C., Minami, K., & Esashi, M. (1995). Silicon resonant angular rate sensor using electromagnetic excitation and capacitive detection. *Journal of Micromechanics and Microengineering*, 5(3), 219.
- [18] Paoletti, F., Gretillat, M. A., & de Rooij, N. F. (1996, February). A silicon micromachined vibrating gyroscope with piezoresistive detection and electromagnetic excitation. In *Micro Electro Mechanical Systems, 1996, MEMS'96, Proceedings. An Investigation of Micro Structures, Sensors, Actuators, Machines and Systems. IEEE, The Ninth Annual International Workshop on* (pp. 162-167). IEEE.
- [19] Boser, B. E., & Howe, R. T. (1996). Surface micromachined accelerometers. *IEEE Journal of solid-state circuits*, 31(3), 366-375.
- [20] An, S., Oh, Y. S., Park, K. Y., Lee, S. S., & Song, C. M. (1999). Dual-axis microgyroscope with closed-loop detection. *Sensors and Actuators A: Physical*, 73(1), 1-6.
- [21] Geiger, W., Folkmer, B., Merz, J., Sandmaier, H., & Lang, W. (1999). A new silicon rate gyroscope. *Sensors and Actuators A: Physical*, 73(1), 45-51.
- [22] Ayazi, F., & Najafi, K. (2001). A HARPSS polysilicon vibrating ring gyroscope. *Journal of microelectromechanical systems*, 10(2), 169-179.

- [23] Zaman, M. F., Sharma, A., & Ayazi, F. (2006). High performance matched-mode tuning fork gyroscope. In *Micro Electro Mechanical Systems, 2006. MEMS 2006 Istanbul. 19th IEEE International Conference on* (pp. 66-69). IEEE.
- [24] Yazdi, N., Ayazi, F., & Najafi, K. (1998). Micromachined inertial sensors. *Proceedings of the IEEE*, 86(8), 1640-1659.
- [25] Niu, M., Xue, W., Wang, X., Xie, J., Yang, G., & Wang, W. (1997, June). Design and characteristics of two-gimbals micro-gyroscopes fabricated with quasi-LIGA process. In *Solid State Sensors and Actuators, 1997. TRANSDUCERS'97 Chicago., 1997 International Conference on* (Vol. 2, pp. 891-894). IEEE.
- [26] Xie, H., & Fedder, G. K. (2003). Fabrication, characterization, and analysis of a DRIE CMOS-MEMS gyroscope. *IEEE Sensors Journal*, 3(5), 622-631.
- [27] Trusov, A., Acar, C., & Shkel, A. M. (2006, March). Comparative analysis of distributed mass micromachined gyroscopes fabricated in SCS-SOI and EFAB. In *Smart Structures and Materials* (pp. 61742A-61742A). International Society for Optics and Photonics.
- [28] Song, C., Ha, B., & Lee, S. (1999). Micromachined inertial sensors. In *Intelligent Robots and Systems, 1999. IROS'99. Proceedings. 1999 IEEE/RSJ International Conference on* (Vol. 2, pp. 1049-1056). IEEE.
- [29] Kraft, M. (2000). Micromachined inertial sensors: The state-of-the-art and a look into the future. *Measurement and Control*, 33(6), 164-168.
- [30] Ward, P. (1996). U.S. Patent No. 5,481,914. Washington, DC: U.S. Patent and Trademark Office.
- [31] Park, S., & Horowitz, R. (2003). Adaptive control for the conventional mode of operation of MEMS gyroscopes. *Journal of Microelectromechanical Systems*, 12(1), 101-108.
- [32] Weinberg, M. S., Kumar, K., & King, A. T. (2003). U.S. Patent No. 6,571,630. Washington, DC: U.S. Patent and Trademark Office.
- [33] Braxmaier, M., Gaier, A., Link, T., Schumacher, A., Simon, I., Frech, J., ... & Lang, W. (2003, June). Cross-coupling of the oscillation modes of vibratory gyroscopes. In *TRANSDUCERS, Solid-State Sensors, Actuators and Microsystems, 12th International Conference on, 2003* (Vol. 1, pp. 167-170). IEEE.

- [34] Alper, S. E., & Akin, T. (2002). A symmetric surface micromachined gyroscope with decoupled oscillation modes. *Sensors and Actuators A: Physical*, 97, 347-358.
- [35] Alper, S. E., & Akin, T. (2004). Symmetrical and decoupled nickel microgyroscope on insulating substrate. *Sensors and Actuators A: Physical*, 115(2), 336-350.
- [36] Alper, S. E., & Akin, T. (2005). A single-crystal silicon symmetrical and decoupled MEMS gyroscope on an insulating substrate. *Journal of Microelectromechanical Systems*, 14(4), 707-717.
- [37] Alper, S. E., Azgin, K., & Akin, T. (2007). A high-performance silicon-on-insulator MEMS gyroscope operating at atmospheric pressure. *Sensors and Actuators A: Physical*, 135(1), 34-42.
- [38] Geiger, W., Merz, J., Fischer, T., Folkmer, B., Sandmaier, H., & Lang, W. (2000). The silicon angular rate sensor system DAVED. *Sensors and Actuators A: Physical*, 84(3), 280-284.
- [39] Geiger, W., Butt, W. U., Gaisser, A., Frech, J., Braxmaier, M., Link, T., ... & Lang, W. (2002). Decoupled microgyros and the design principle DAVED. *Sensors and Actuators A: Physical*, 95(2), 239-249.
- [40] Painter, C. C., & Shkel, A. M. (2003). Active structural error suppression in MEMS vibratory rate integrating gyroscopes. *IEEE Sensors Journal*, 3(5), 595-606.
- [41] Painter, C. C., & Shkel, A. M. (2003). Structural and thermal modeling of a z-axis rate integrating gyroscope. *Journal of Micromechanics and Microengineering*, 13(2), 229.
- [42] Acar, C., & Shkel, A. M. (2003). Nonresonant micromachined gyroscopes with structural mode-decoupling. *IEEE Sensors Journal*, 3(4), 497-506.
- [43] Ghommem, M., Nayfeh, A. H., Choura, S., Najjar, F., & Abdel-Rahman, E. M. (2010). Modeling and performance study of a beam microgyroscope. *Journal of Sound and Vibration*, 329(23), 4970-4979.
- [44] Acar, C., & Shkel, A. M. (2005). An approach for increasing drive-mode bandwidth of MEMS vibratory gyroscopes. *Journal of microelectromechanical systems*, 14(3), 520-528.

- [45] Schofield, A. R., Trusov, A. A., Acar, C., & Shkel, A. M. (2007, June). Anti-phase driven rate gyroscope with multi-degree of freedom sense mode. In *Solid-State Sensors, Actuators and Microsystems Conference, 2007. TRANSDUCERS 2007. International* (pp. 1199-1202). IEEE.
- [46] Oropeza-Ramos, L. A., Burgner, C. B., & Turner, K. L. (2008, January). Inherently robust micro gyroscope actuated by parametric resonance. In *Micro Electro Mechanical Systems, 2008. MEMS 2008. IEEE 21st International Conference on* (pp. 872-875). IEEE.
- [47] Petersen, K. E., Maluf, N., McCulley, W., Logan, J., Klaasen, E., & Noworolski, J. M. (2000). U.S. Patent No. 6,084,257. Washington, DC: U.S. Patent and Trademark Office. Chicago
- [48] Laermer, F., & Schilp, A. (1996). U.S. Patent No. 5,501,893. Washington, DC: U.S. Patent and Trademark Office.
- [49] Zaman, M., Sharma, A., Amini, B., & Ayazi, F. (2004, June). Towards inertial grade vibratory microgyros: A high-Q in-plane silicon-on-insulator tuning fork device. In *Proceedings of Solid-State Sensor, Actuator and Microsystems Workshop, Hilton Head Island, SC, USA* (pp. 6-10).
- [50] Sharma, A., Zaman, F. M., Amini, B. V., & Ayazi, F. (2004, October). A high-Q in-plane SOI tuning fork gyroscope. In *Sensors, 2004. Proceedings of IEEE* (pp. 467-470). IEEE.
- [51] Acar, C., & Shkel, A. M. (2004, October). Post-release capacitance enhancement in micromachined devices. In *Sensors, 2004. Proceedings of IEEE* (pp. 268-271). IEEE.
- [52] Lee, S., Park, S., & Cho, D. I. (1999). The surface/bulk micromachining (SBM) process: a new method for fabricating released MEMS in single crystal silicon. *Journal of Microelectromechanical Systems*, 8(4), 409-416.
- [53] Lee, S., Park, S., Kim, J., Lee, S., & Cho, D. I. (2000). Surface/bulk micromachined single-crystalline-silicon micro-gyroscope. *Journal of Microelectromechanical Systems*, 9(4), 557-567.
- [54] Kim, J., Park, S., Kwak, D., Ko, H., & Cho, D. I. D. (2005). An x-axis single-crystalline silicon microgyroscope fabricated by the extended SBM process. *Journal of microelectromechanical systems*, 14(3), 444-455.

- [55] Alper, S. E., Ocak, I. E., & Akin, T. (2007). Ultrathick and high-aspect-ratio nickel microgyroscope using EFAB multilayer additive electroforming. *Journal of Microelectromechanical Systems*, 16(5), 1025-1035.
- [56] Yang, K., Zhou, J., & Yan, G. (2004, October). The research on MEMS fang-bar fluidic angular rate sensor. In *Solid-State and Integrated Circuits Technology, 2004. Proceedings. 7th International Conference on* (Vol. 3, pp. 1808-1811). IEEE.
- [57] Zhou, J., Yan, G., Zhu, Y., Xiao, Z., & Fan, J. (2005). Design and fabrication of a microfluid angular rate sensor. In *Micro Electro Mechanical Systems, 2005. MEMS 2005. 18th IEEE International Conference on* (pp. 363-366). IEEE.
- [58] Dau, V. T., Dinh, T. X., Dao, D. V., Tomonori, O., & Sugiyama, S. (2007, October). Design and fabrication of a convective 3-DOF angular rate sensor. In *Sensors, 2007 IEEE* (pp. 915-918). IEEE. Chicago
- [59] Varadan, V. K., Suh, W. D., Xavier, P. B., Jose, K. A., & Varadan, V. V. (2000). Design and development of a MEMS-IDT gyroscope. *Smart Materials and Structures*, 9(6), 898.
- [60] Lajimi, S. A. M., Heppler, G. R., & Abdel-Rahman, E. (2014, April). The application of a new beam-rigid body mems gyroscope in the frequency-modulation mode. In *Nano/Micro Engineered and Molecular Systems (NEMS), 2014 9th IEEE International Conference on* (pp. 586-591). IEEE.
- [61] Effa, D., Abdel-Rahman, E., & Yavuz, M. (2013, July). Cantilever beam microgyroscope based on frequency modulation. In *Advanced Intelligent Mechatronics (AIM), 2013 IEEE/ASME International Conference on* (pp. 844-849). IEEE.
- [62] Reddy, J. N. (2014). *An Introduction to Nonlinear Finite Element Analysis: with applications to heat transfer, fluid mechanics, and solid mechanics*. OUP Oxford.
- [63] Kovacs, G. T. (1998). *Micromachined transducers sourcebook* (pp. 586-587). New York: WCB/McGraw-Hill.
- [64] Acar, C., & Shkel, A. (2008). *MEMS vibratory gyroscopes: structural approaches to improve robustness*. Springer Science & Business Media.
- [65] Carter, J., Cowen, A., Hardy, B., Mahadevan, R., Stonefield, M., & Wilcenski, S. (2005). *PolyMUMPs design handbook*. MEMSCAP Inc., Revision, 11.